ACADEMIC PRESS

Available online at www.sciencedirect.com

SCIENCE DIRECT®

Journal of Computational Physics 185 (2003) 445–471

JOURNAL OF COMPUTATIONAL PHYSICS

www.elsevier.com/locate/jcp

An Eulerian description of the streaming process in the lattice Boltzmann equation

Taehun Lee, Ching-Long Lin *

Department of Mechanical and Industrial Engineering, IIHR – Hydroscience and Engineering, The University of Iowa, Iowa City, IA 52242-1527, USA

Received 4 April 2002; received in revised form 16 September 2002; accepted 6 November 2002

Abstract

This paper presents a novel strategy for solving discrete Boltzmann equation (DBE) for simulation of fluid flows. This strategy splits the solution procedure into streaming and collision steps as in the lattice Boltzmann equation (LBE) method. The streaming step can then be carried out by solving pure linear advection equations in an Eulerian framework. This offers two significant advantages over previous methods. First, the relationship between the relaxation parameter and the discretization of the collision term developed from the LBE method is directly applicable to the DBE method. The resulting DBE collision step remains local and poses no constraint on time step. Second, decoupling of the advection step from the collision step facilitates implicit discretization of the advection equation on arbitrary meshes. An implicit unstructured DBE method is constructed based on this strategy and is evaluated using several test cases of flow over a backward-facing step, lid-driven cavity flow, and flow past a circular cylinder. The speedup of convergence for some cases improves by a factor of about 20.

Keywords: Lattice Boltzmann equation; Unstructured mesh; Implicit scheme

1. Introduction

The conventional lattice Boltzmann equation (LBE) method [1] comprises collision and streaming steps. In the collision step the particle distribution function is updated at regularly spaced lattice points. In the streaming step the particle distribution function is shifted perfectly between lattice points, involving neither phase nor amplitude error. This greatly facilitates numerical procedure, but limits shapes of computational domain due to the coupled space–time discretization of the method. The coupling could substantially increase computational effort for flows of boundary-layer type and in complex geometries.

* Corresponding author. Tel.: 1-319-335-5673; fax: 1-319-335-5669.
E-mail address: ching-long-lin@uiowa.edu (C.-L. Lin).

0021-9991/02/$ - see front matter
doi:10.1016/S0021-9991(02)00065-7

To overcome the geometric constraint of the LBE method, several discrete Boltzmann equation (DBE) methods have been proposed [2–6]. They are based on direct discretization of the DBE [7] in space and time using standard discretization schemes, such as finite difference, finite volume, and finite element methods. The starting point of these methods is the differential DBE with the λ–v relation given as $v = \lambda c_s^2$, where λ is the relaxation parameter, v is the kinematic viscosity, and c_s is the speed of sound. It should be recognized that this λ–v relation is only valid for the differential form of the DBE to recover the Navier–Stokes equations. It may not be applied to the difference equations resulting from discretization of the DBE. Correction to this relation is required to accurately recover the Navier–Stokes equations from various difference equations. Although the correction of the λ–v relation is well known in the conventional LBE method, it is overlooked in developing the DBE methods. That is, use of the explicit Euler, Crank–Nicolson, and implicit Euler methods for the collision term requires different λ–v relations.

Since the relationship between the relaxation parameter and the discretization of the collision term is already established in the LBE method, it is natural to relate the LBE method to the DBE method and incorporate some advantages of the LBE method into the solution procedure of the DBE. The LBE can be regarded as a special space–time discretization of the DBE along characteristics and comprises streaming and collision steps. The streaming step can be interpreted as moving particle distribution functions along characteristics between nodes, and is viewed as an Lagrangian description of the advection of fluid particles. As for the collision step, explicit and implicit schemes have no effect on the overall performance of the method if a proper relaxation parameter is used. As a rule, discretization of the collision term and the choice of the relaxation parameter are such that the overall scheme is second-order accurate in space and time.

From an Eulerian point of view, the aforementioned streaming step is equivalent to solving a pure linear advection equation for the field of particle distribution function. Thus if the solution procedure of the DBE is also split into the two steps, the advection equation in principle can be solved by any second-order accurate scheme on arbitrary meshes. The treatment of the collision then remains identical to that of the LBE method. This strategy offers two significant advantages over the previous DBE methods. First, the relationship between the relaxation parameter and the discretization of the collision term developed from the LBE method is directly applicable to the DBE method. The resulting DBE collision step also inherits the feature of localization as in the LBE method. Second, decoupling of the advection step from the collision step in the DBE method allows implicit discretization of the advection equation on unstructured meshes in a simple fashion.

In this paper, we present the above strategy for solving the DBE and investigate the following questions. First, what is the correct λ–v relation for the popular θ method having second-order accuracy in the DBE? $\theta = 0$, 0.5, and 1 correspond to the explicit Euler, Crank–Nicolson, and implicit Euler methods. Second, what are the stability properties of these methods? Third, how can one improve the stability of the DBE method and use much larger Courant–Friedrichs–Lewy (*CFL*) numbers than unity and time step sizes? Fourth, what is the relationship between the present scheme and several previous DBE methods? Fifth, what is the appropriate boundary condition for the present implicit scheme? On these bases, an implicit unstructured DBE method is constructed to demonstrate numerically the features of the new solution procedure.

The paper is organized as follows. In Section 2, we derive a general λ–v relation and elucidate the concepts that the new DBE method is based upon. A new boundary condition for the current method is presented. Section 3 begins with a linear stability analysis of the collision term treated by the θ method. We then compare the current DBE method with other existing methods. In Section 4, we apply the implicit Taylor–Galerkin finite element method [8,9] to the pure advection equation to achieve larger time step on either nonuniform or unstructured meshes. In Section 5, several test cases of flow over a backward-facing step, lid-driven cavity flow, and flow past a circular cylinder are considered and compared with benchmark data. Concluding remarks are made in Section 6.

2. Eularian description of the LBE

The DBE [7] with the Bhatnagar–Gross–Krook (BGK) collision operator [10] reads

$$\frac{\partial f_\alpha}{\partial t} + \mathbf{e}_\alpha \cdot \nabla f_\alpha = -\frac{1}{\lambda}(f_\alpha - f_\alpha^{\mathrm{eq}}), \tag{1}$$

where f_α is the single-particle distribution function, $\mathbf{e}_\alpha$ is the discrete microscopic velocity, ∇f_α is the gradient of f_α, λ is the relaxation parameter of collision, and f_α^{eq} is the equilibrium distribution function obtained by Taylor expanding Maxwell–Boltzmann distribution function up to $(\mathbf{u}\cdot\mathbf{u})$. If a nine-velocity LBE model on a square lattice is used, the discrete velocity $\mathbf{e}_\alpha$ is expressed as

$$\mathbf{e}_\alpha = \begin{cases} (0,0), & \alpha = 0, \\ (\cos\theta_\alpha, \sin\theta_\alpha), \quad \theta_\alpha = (\alpha-1)\pi/4, & \alpha = 1,3,5,7, \\ \sqrt{2}(\cos\theta_\alpha, \sin\theta_\alpha), \quad \theta_\alpha = (\alpha-1)\pi/4, & \alpha = 2,4,6,8. \end{cases} \tag{2}$$

The equilibrium distribution function f_α^{eq} takes the form.

$$f_\alpha^{\mathrm{eq}} = w_\alpha \rho \left[1 + 3\mathbf{e}_\alpha\cdot\mathbf{u} + \frac{9}{2}(\mathbf{e}_\alpha\cdot\mathbf{u})^2 - \frac{3}{2}(\mathbf{u}\cdot\mathbf{u})\right] \tag{3}$$

with the weights $w_0 = 4/9$, $w_1 = w_3 = w_5 = w_7 = 1/9$, and $w_2 = w_4 = w_6 = w_8 = 1/36$ [11]. The macroscopic density ρ and the velocity vector $\mathbf{u}$ are related to the distribution function by

$$\sum_{\alpha=0}^{8} f_\alpha^{\mathrm{eq}} = \sum_{\alpha=0}^{8} f_\alpha = \rho, \quad \sum_{\alpha=1}^{8} \mathbf{e}_\alpha f_\alpha^{\mathrm{eq}} = \sum_{\alpha=1}^{8} \mathbf{e}_\alpha f_\alpha = \rho\mathbf{u}. \tag{4}$$

The pressure can be calculated from $p = c_s^2\rho$ with the speed of sound $c_s = 1/\sqrt{3}$ and the kinematic viscosity of fluid is $v = \lambda c_s^2$. Mach (Ma) number is defined as U/c_s, where U is the characteristic velocity of the system.

2.1. Lattice Boltzmann equation

Let $\tilde{\mathbf{x}}(t)$ denote the trajectory of the particle. Eq. (1) then can be written as

$$\frac{D}{Dt} f_\alpha(\tilde{\mathbf{x}}(t), t) = -\frac{1}{\lambda}\left[f_\alpha(\tilde{\mathbf{x}}(t), t) - f_\alpha^{\mathrm{eq}}(\tilde{\mathbf{x}}(t), t)\right], \tag{5}$$

where $D/Dt \equiv \partial/\partial t + \mathbf{e}_\alpha\cdot\nabla$ is the Lagrangian derivative along characteristics.

Suppose that the solution at the time t_n is known. To compute the solution at the time t_{n+1}, we discretize Eq. (5) along characteristics using the θ method [12].

$$\begin{aligned} f_\alpha\left(\tilde{\mathbf{x}}(t_{n+1}), t_{n+1}\right) - f_\alpha\left(\tilde{\mathbf{x}}(t_n), t_n\right) = & -\theta_c \frac{\Delta t}{\lambda}\left[f_\alpha\left(\tilde{\mathbf{x}}(t_{n+1}), t_{n+1}\right) - f_\alpha^{\mathrm{eq}}\left(\tilde{\mathbf{x}}(t_{n+1}), t_{n+1}\right)\right] \\ & - (1-\theta_c)\frac{\Delta t}{\lambda}\left[f_\alpha\left(\tilde{\mathbf{x}}(t_n), t_n\right) - f_\alpha^{\mathrm{eq}}\left(\tilde{\mathbf{x}}(t_n), t_n\right)\right], \end{aligned} \tag{6}$$

where $t_{n+1} = t_n + \Delta t$, $\tilde{\mathbf{x}}(t_{n+1}) = \tilde{\mathbf{x}}(t_n) + \Delta t\mathbf{e}_\alpha$, and $\theta_c \in [0,1]$. According to accuracy analysis of an ordinary differential equation, θ_c must be set to 0.5 for second-order accuracy (i.e., the Crank–Nicolson method). In the LBE method, one can actually choose any value of $\theta_c \in [0,1]$ while retaining second-order accuracy as long as the relaxation parameter satisfies

$$v = (\lambda/\Delta t - 0.5 + \theta_c)c_s^2\Delta t. \tag{7}$$

As shown in Appendix A, the principal truncation error $O(\Delta t)$ in the Chapman–Enskog expansion of Eq. (6) for recovering the Navier–Stokes equations is gone if Eq. (7) is satisfied. It is well known in the conventional LBE, viz. Eq. (6) with $\theta_c = 0$, that satisfaction of Eq. (7) warrants second-order temporal accuracy. Nevertheless, the implicit treatment of the collision term with $\theta_c \neq 0$ should also satisfy the above constraint, but being overlooked. Hereafter, we call the schemes using $\theta_c = 0$ *collision-explicit* (CE), and those with $0 < \theta_c \leqslant 1$ *collision-implicit* (CI). The stability properties of the CE and CI schemes will be discussed later.

To solve the LBE Eq. (6), we regroup f_α at the t_{n+1} time level on one side and f_α at t_n on the other, and split the solution procedure into the following steps.

- Pre-streaming collision step

$$\hat{f}_\alpha(\tilde{\mathbf{x}}(t_n), t_n) = f_\alpha(\tilde{\mathbf{x}}(t_n), t_n) - (1-\theta_c)\frac{\Delta t}{\lambda}\left[f_\alpha(\tilde{\mathbf{x}}(t_n), t_n) - f_\alpha^{eq}(\tilde{\mathbf{x}}(t_n), t_n)\right]. \tag{8}$$

- Streaming step

$$\hat{f}_\alpha(\tilde{\mathbf{x}}(t_{n+1}), t_{n+1}) = \hat{f}_\alpha(\tilde{\mathbf{x}}(t_n), t_n). \tag{9}$$

- Post-streaming collision step

$$\hat{f}_\alpha(\tilde{\mathbf{x}}(t_{n+1}), t_{n+1}) = f_\alpha(\tilde{\mathbf{x}}(t_{n+1}), t_{n+1}) + \theta_c\frac{\Delta t}{\lambda}\left[f_\alpha(\tilde{\mathbf{x}}(t_{n+1}), t_{n+1}) - f_\alpha^{eq}(\tilde{\mathbf{x}}(t_{n+1}), t_{n+1})\right]. \tag{10}$$

Eq. (10) can be readily rearranged as

$$f_\alpha(\tilde{\mathbf{x}}(t_{n+1}), t_{n+1}) = \left[\hat{f}_\alpha(\tilde{\mathbf{x}}(t_{n+1}), t_{n+1}) + \theta_c\frac{\Delta t}{\lambda}f_\alpha^{eq}(\tilde{\mathbf{x}}(t_{n+1}), t_{n+1})\right] \Big/ \left[1 + \theta_c\frac{\Delta t}{\lambda}\right]. \tag{11}$$

The macroscopic density and velocities used in calculation of f_α^{eq} in Eq. (11) are obtained by taking moments of $\hat{f}_\alpha$ at t_{n+1}.

$$\rho = \sum_{\alpha=0}^{8}\hat{f}_\alpha, \quad \rho\mathbf{u} = \sum_{\alpha=1}^{8}\mathbf{e}_\alpha\hat{f}_\alpha. \tag{12}$$

In practice, it is computationally efficient to combine the pre-streaming collision and the post-streaming collision steps as in [13].

2.2. Eulerian description of streaming

In the conventional LBE method the grid points coincide with lattice points and the streaming step expressed by Eq. (9) becomes a perfect shift. The streaming step can be regarded as a Lagrangian approach in that a group of particles represented by the particle distribution function move along characteristics. The perfect shift poses no stability and accuracy issues because it involves neither phase nor amplitude error (known as neutral stability). The *CFL* number for perfect shift equals unity, which couples grid distance and time step. As a result, large time step is achieved at the expense of spatial resolution.

The Lagrangian description of the LBE given by Eqs. (8)–(10) can alternatively be expressed in an Eulerian framework shown below.

- Pre-streaming collision step

$$\hat{f}_\alpha(\mathbf{x}, t_n) = f_\alpha(\mathbf{x}, t_n) - (1-\theta_c)\frac{\Delta t}{\lambda}\left[f_\alpha(\mathbf{x}, t_n) - f_\alpha^{eq}(\mathbf{x}, t_n)\right]. \tag{13}$$

- Streaming step

$$\frac{\partial \hat{f}_\alpha}{\partial t} + \mathbf{e}_\alpha \cdot \nabla \hat{f}_\alpha = 0. \tag{14}$$

- Post-streaming collision step

$$\hat{f}_\alpha(\mathbf{x}, t_{n+1}) = f_\alpha(\mathbf{x}, t_{n+1}) + \theta_c \frac{\Delta t}{\lambda}\left[f_\alpha(\mathbf{x}, t_{n+1}) - f_\alpha^{eq}(\mathbf{x}, t_{n+1})\right]. \tag{15}$$

Here $\mathbf{x}$ is defined at grid points not necessarily lining up along characteristics. The above streaming step Eq. (14) can be solved virtually by any second-order accurate scheme suited for the pure advection equation, e.g., the Lax–Wendroff-type schemes, to replace the perfect shift in the conventional LBE method. As shown in Appendix A, use of a second-order time accurate scheme for the streaming step is essential in recovering the Navier–Stokes equations to the second-order accuracy in time. The stability limit then is determined by the scheme applied to Eq. (14). Because of the Eulerian nature of Eq. (14), the space and time discretizations are decoupled, allowing control of time step irrespective of spatial resolution and geometric shape of the problem.

2.3. Boundary condition

In the solution procedure described by Eqs. (13)–(15), only the streaming step requires boundary conditions because there is no spatial derivative of f_α in the two collision steps. The streaming step given by Eq. (14) is hyperbolic and therefore, boundary conditions must be provided if $\mathbf{e}_\alpha \cdot \mathbf{n} < 0$ where $\mathbf{n}$ is a unit vector outward normal to the local boundary surface. On the other hand, if $\mathbf{e}_\alpha \cdot \mathbf{n} > 0$, boundary conditions are not necessary so that either one-sided difference or simple extrapolation scheme suffices. Suppose $\hat{f}_\alpha(\mathbf{x})$ is to be evaluated at the domain boundary point $\mathbf{x}$ and $\mathbf{e}_\alpha \cdot \mathbf{n} < 0$ at $\mathbf{x}$. If $\hat{f}_\beta(\mathbf{x})$ moves in the opposite direction of $\hat{f}_\alpha(\mathbf{x})$, i.e., $\mathbf{e}_\beta = -\mathbf{e}_\alpha$, and $\mathbf{e}_\beta \cdot \mathbf{n} > 0$, the boundary condition for $\hat{f}_\alpha(\mathbf{x})$ can be specified through $\hat{f}_\beta(\mathbf{x})$, or alternatively, through $f_\beta(\mathbf{x})$ and $f_\beta^{eq}(\mathbf{x})$.

We shall start with the bounce-back rule of the nonequilibrium distribution proposed by He et al. [14]. It takes the form of

$$\left(f_\alpha - f_\alpha^{eq}\right) - \left(f_\beta - f_\beta^{eq}\right) = 0. \tag{16}$$

The discussion on the physical meaning of Eq. (16) can be found in [14]. This boundary condition is of second-order accuracy. Since the only variable in the streaming step Eq. (14) is $\hat{f}_\alpha$, a variant of the boundary condition Eq. (16) in terms of $\hat{f}_\alpha$ and $\hat{f}_\beta$ is proposed.

$$\left(\hat{f}_\alpha^{n+1} - \hat{f}_\alpha^{n}\right) - \left(\hat{f}_\beta^{n+1} - \hat{f}_\beta^{n}\right) = 0. \tag{17}$$

This boundary condition recovers Eq. (16) in the incompressible limit as shown below. It has several features, including second-order accuracy, easy implementation for implicit schemes, and strong coupling between $\hat{f}_\alpha$ and $\hat{f}_\beta$ at the boundary nodes. Replacing $\hat{f}_\alpha$ and $\hat{f}_\beta$ in Eq. (17) by Eqs. (13) and (15) yields

$$\begin{aligned}&\left(f_\alpha^{n+1} - f_\alpha^{n}\right) + \theta_c \frac{\Delta t}{\lambda}\left(f_\alpha^{n+1} - f_\alpha^{eq,n+1}\right) + (1-\theta_c)\frac{\Delta t}{\lambda}\left(f_\alpha^{n} - f_\alpha^{eq,n}\right) - \left(f_\beta^{n+1} - f_\beta^{n}\right) - \theta_c \frac{\Delta t}{\lambda}\left(f_\beta^{n+1} - f_\beta^{eq,n+1}\right)\\ &\quad - (1-\theta_c)\frac{\Delta t}{\lambda}\left(f_\beta^{n} - f_\beta^{eq,n}\right) = 0.\end{aligned} \tag{18}$$

Use of the relation Eq. (16) leads to

$$\left(f_\alpha^{\mathrm{eq},n+1}-f_\beta^{\mathrm{eq},n+1}\right)-\left(f_\alpha^{\mathrm{eq},n}-f_\beta^{\mathrm{eq},n}\right)+\theta_c\frac{\Delta t}{\lambda}\left(f_\alpha^{n+1}-f_\alpha^{\mathrm{eq},n+1}\right)-\theta_c\frac{\Delta t}{\lambda}\left(f_\beta^{n+1}-f_\beta^{\mathrm{eq},n+1}\right)$$
$$+(1-\theta_c)\frac{\Delta t}{\lambda}\left(f_\alpha^{n}-f_\alpha^{\mathrm{eq},n}\right)-(1-\theta_c)\frac{\Delta t}{\lambda}\left(f_\beta^{n}-f_\beta^{\mathrm{eq},n}\right)=0. \tag{19}$$

Due to the symmetry of the model, we can use Eq. (3) to simplify the first two terms in the brackets to

$$\mathrm{sign}(\mathbf{e}_\alpha)6w_\alpha\left(\rho^{n+1}-\rho^n\right)\mathbf{U}, \tag{20}$$

where $\mathbf{U}$ is the velocity prescribed at boundaries. Usually the density variation in time is very small on the order of Ma^2. Thus in the incompressible limit, Eq. (19) recovers the bounce-back rule of the nonequilibrium distribution. If the incompressible LBE model [15] is used instead, Eq. (20) exactly becomes zero and the proposed boundary condition is identical to the bounce-back rule of the nonequilibrium distribution. In any case, boundary conditions for the macroscopic variables, such as velocities and density, must be provided for evaluation of the equilibrium distribution function.

It is noteworthy that even without imposing the above boundary condition at the nodes where $\mathbf{e}_\alpha\cdot\mathbf{n}<0$, one-sided difference [3,6] works moderately well. The reason might be that the original DBE is not a pure advection equation but an advection equation with the collision term, whose diffusive effect tends to stabilize the scheme. The stability of the one-sided difference approach alone, however, deteriorates as the *Re* number increases.

3. Comparison with other methods

3.1. Time-step constraints for CI/CE schemes

In order to compare with other schemes, we shall first examine the stability properties of the collision term. For simplicity, let us consider a one-dimensional ordinary differential equation for the collision step to illustrate that proper discretization of the collision term poses no constraint on time step. It will then lead to the conclusion that a larger time step or *CFL* number could be used if a more stable method is used to solve the advection equation in the streaming step.

A simple one-dimensional model equation for the collision reads

$$\frac{\mathrm{d}f_\alpha}{\mathrm{d}t}=-\frac{1}{\lambda}f_\alpha+\frac{1}{\lambda}f_\alpha^{\mathrm{eq}}. \tag{21}$$

The equilibrium distribution function f_α^{eq} poses challenges in stability analysis of this equation due to its nonlinear nature. There are two ways to handle it. First, linearization of various form is applied to the nonlinear term as in [16]. Second, time splitting Eq. (21) again permits to analyze the stability of the first term on the right-hand side of the equation. This is equivalent to treating the f_α^{eq} term as a source term and assuming its weak dependence on f_α. We adopt this approach for the following analysis. Analogous to the analysis of a strictly autonomous system, the stability primarily depends on the transient, homogeneous part of the solution which satisfies

$$\frac{\mathrm{d}f_\alpha}{\mathrm{d}t}=-\frac{1}{\lambda}f_\alpha. \tag{22}$$

As indicated in [12], the linear stability condition thus derived is only a necessary one, requiring numerical experiments for validation. With this in mind, we discretize Eq. (22) using the θ method to obtain

$$f_\alpha^{n+1}-f_\alpha^n=-\frac{\Delta t\theta_c}{\lambda}f_\alpha^{n+1}-\frac{\Delta t(1-\theta_c)}{\lambda}f_\alpha^n \tag{23}$$

with $\theta_c \in [0,1]$. This is easily rearranged to give

$$f_\alpha^{n+1} = \left[\frac{1-\Delta t(1-\theta_c)/\lambda}{1+\Delta t\theta_c/\lambda}\right] f_\alpha^n, \tag{24}$$

where the term in the square brackets is known as an amplification factor. Numerical stability requires the amplitude of the factor less than or equal to unity.

$$\left|\frac{1-\Delta t(1-\theta_c)/\lambda}{1+\Delta t\theta_c/\lambda}\right| \leqslant 1. \tag{25}$$

Recall that Eq. (7) must be satisfied to recover the Navier–Stokes equations to second-order accuracy in time. Substitution of Eq. (7) into the amplification factor gives

$$\left|\frac{1-\Delta t(1-\theta_c)/\lambda}{1+\Delta t\theta_c/\lambda}\right| = \left|\frac{1-\frac{(1-\theta_c)}{v/c_s^2\Delta t+0.5-\theta_c}}{1+\frac{\theta_c}{v/c_s^2\Delta t+0.5-\theta_c}}\right| = \left|\frac{\frac{v}{c_s^2\Delta t}-0.5}{\frac{v}{c_s^2\Delta t}+0.5}\right| < 1. \tag{26}$$

Two immediate conclusions can be drawn from this result. First, the transient solution to the model equation for the collision is unconditionally stable for any values of θ_c. That is, both the CE and CI schemes based on the θ method are unconditionally stable if Eq. (7) is satisfied. Second, oscillatory solution may be produced as the amplification factor approaches negative unity [17]. This occurs when the kinematic viscosity v becomes small at high Reynolds (Re) number or the time step becomes large.

3.2. Comparisons of different schemes

We next apply the Lax–Wendroff scheme to approximate Eq. (14) and compare it with other methods.

$$\frac{\hat{f}_\alpha^{n+1}-\hat{f}_\alpha^n}{\Delta t} = -e_{\alpha r}\frac{\partial \hat{f}_\alpha^n}{\partial x_r} + \frac{\Delta t}{2}e_{\alpha s}\frac{\partial}{\partial x_s}e_{\alpha r}\frac{\partial}{\partial x_r}\hat{f}_\alpha^n. \tag{27}$$

The Chapman–Enskog expansion of the scheme along with the collision steps leads to the Navier–Stokes equations (see Appendix A). By combining the collision and streaming steps, we obtain

$$\begin{aligned} f_\alpha^{n+1}-f_\alpha^n = &-\Delta t\left[e_{\alpha r}\frac{\partial f_\alpha^n}{\partial x_r} + \frac{(1-\theta_c)}{\lambda}\left(f_\alpha - f_\alpha^{eq}\right)^n + \frac{\theta_c}{\lambda}\left(f_\alpha - f_\alpha^{eq}\right)^{n+1}\right] + \Delta t^2 e_{\alpha s}\frac{\partial}{\partial x_s}\left[\frac{1}{2}e_{\alpha r}\frac{\partial f_\alpha^n}{\partial x_r}\right. \\ &\left. + \frac{(1-\theta_c)}{\lambda}\left(f_\alpha - f_\alpha^{eq}\right)^n\right] - \frac{\Delta t^3}{2}\frac{(1-\theta_c)}{\lambda}e_{\alpha s}\frac{\partial}{\partial x_s}\left[e_{\alpha r}\frac{\partial}{\partial x_r}\left(f_\alpha - f_\alpha^{eq}\right)^n\right]. \end{aligned} \tag{28}$$

For comparison with other methods, we choose $\theta_c = 0$, 0.5, and 1. They correspond to the explicit Euler, Crank–Nicolson, and implicit Euler discretization of the collision step, respectively.

3.2.1. Explicit Euler method

For $\theta_c = 0$, Eq. (28) is the Lax–Wendroff counterpart of the conventional LBE.

$$\begin{aligned} f_\alpha^{n+1}-f_\alpha^n = &-\Delta t\left[e_{\alpha r}\frac{\partial f_\alpha^n}{\partial x_r} + \frac{1}{\lambda}\left(f_\alpha - f_\alpha^{eq}\right)^n\right] + \Delta t^2 e_{\alpha s}\frac{\partial}{\partial x_s}\left[\frac{1}{2}e_{\alpha r}\frac{\partial f_\alpha^n}{\partial x_r} + \frac{1}{\lambda}\left(f_\alpha - f_\alpha^{eq}\right)^n\right] \\ &-\frac{\Delta t^3}{2}\frac{1}{\lambda}e_{\alpha s}\frac{\partial}{\partial x_s}\left[e_{\alpha r}\frac{\partial}{\partial x_r}\left(f_\alpha - f_\alpha^{eq}\right)^n\right]. \end{aligned} \tag{29}$$

The last term on the right-hand side is apparently proportional to Δt^3 but it is still $O(\Delta t^2)$ since λ is $O(\Delta t)$ for small viscosity (i.e., $\lambda = v/c_s^2 + 0.5\Delta t$). Thus it cannot be dropped from the formulation.

The Lax–Wendroff LBE method applied in the 1-D characteristic direction has been proposed by McNamara et al. [18] to stabilize the thermal LBE method. Later, it is known to eliminate staggered invariants of the conventional LBE method [19]. In two-dimensional Cartesian and curvilinear coordinates, He et al. [20,21] used the second-order upwind interpolation after the streaming step in their interpolation-supplemented LBE method.

3.2.2. Crank–Nicolson method

For $\theta_c = 0.5$, Eq. (28) reduces to

$$f_\alpha^{n+1} - f_\alpha^n = -\Delta t\left[e_{\alpha r}\frac{\partial f_\alpha^n}{\partial x_r} + \frac{1}{2\lambda}\left(f_\alpha - f_\alpha^{eq}\right)^n + \frac{1}{2\lambda}\left(f_\alpha - f_\alpha^{eq}\right)^{n+1}\right] + \Delta t^2 e_{\alpha s}\frac{\partial}{\partial x_s}\left[\frac{1}{2}e_{\alpha r}\frac{\partial f_\alpha^n}{\partial x_r} + \frac{1}{2\lambda}\left(f_\alpha - f_\alpha^{eq}\right)^n\right] - \frac{\Delta t^3}{2}\frac{1}{2\lambda}e_{\alpha s}\frac{\partial}{\partial x_s}\left[e_{\alpha r}\frac{\partial}{\partial x_r}\left(f_\alpha - f_\alpha^{eq}\right)^n\right]. \tag{30}$$

This equation differs from the modified equation in [6] only by the last term on the right-hand side. However, this term is $O(\Delta t^3)$ because $\lambda = \nu/c_s^2$ is of O(1), and is negligible as compared with other terms. Cao et al. [2] and Teng et al. [22] used the second-order Runge–Kutta time-stepping scheme for the DBE (RK2-DBE hereafter). The second-order central difference and the total variation diminishing spatial discretization were used for the advection term, respectively. In their methods, the collision term was treated as an explicit source term and the relationship between the relaxation parameter and the kinematic viscosity was given as $\lambda = \nu/c_s^2$. In two-step form their schemes can be written as

- Predictor

$$f_\alpha^{n+1/2} - f_\alpha^n = -\frac{\Delta t}{2}\left[e_{\alpha r}\frac{\partial f_\alpha^n}{\partial x_r} + \frac{1}{\lambda}\left(f_\alpha - f_\alpha^{eq}\right)^n\right]. \tag{31}$$

- Corrector

$$f_\alpha^{n+1} - f_\alpha^n = -\Delta t\left[e_{\alpha r}\frac{\partial f_\alpha^{n+1/2}}{\partial x_r} + \frac{1}{\lambda}\left(f_\alpha - f_\alpha^{eq}\right)^{n+1/2}\right]. \tag{32}$$

Simply put, it can be rearranged in one-step form.

$$f_\alpha^{n+1} - f_\alpha^n = -\Delta t\left[e_{\alpha r}\frac{\partial f_\alpha^n}{\partial x_r} + \frac{1}{\lambda}\left(f_\alpha - f_\alpha^{eq}\right)^{n+1/2}\right] + \frac{\Delta t^2}{2}e_{\alpha s}\frac{\partial}{\partial x_s}\left[e_{\alpha r}\frac{\partial f_\alpha^n}{\partial x_r} + \frac{1}{\lambda}\left(f_\alpha - f_\alpha^{eq}\right)^n\right]. \tag{33}$$

Comparison with Eq. (30) shows that the $O(\Delta t^3)$ term is absent in Eq. (33) and the collision term of Eq. (33) is evaluated explicitly in the predictor step at the $t_{n+1/2}$ time level. Most importantly, the stability property of the scheme is totally changed as illustrated below.

Following the analysis in Section 3.1 that leads to Eq. (25), we apply the second-order Runge–Kutta method to Eq. (22).

$$f_\alpha^{n+1} - f_\alpha^n = -\frac{\Delta t}{\lambda}f_\alpha^n + \frac{\Delta t^2}{2\lambda^2}f_\alpha^n. \tag{34}$$

It is instructive to compare this equation with Eq. (23) obtained by the θ method. The stability of the scheme based on the amplitude of amplification factor requires

$$\left|1 - \frac{\Delta t}{\lambda} + \frac{\Delta t^2}{2\lambda^2}\right| \leqslant 1, \tag{35}$$

which easily leads to

$$\Delta t < 2\lambda = 2\nu/c_s^2. \tag{36}$$

This indicates that the time step is severely restricted as the *Re* number increases. To overcome this stability limit, one may apply the Runge–Kutta time-stepping to the pure advection equation Eq. (14) and apply the θ method to the collision steps with the correct λ–ν relation Eq. (7). However, the second-order Runge–Kutta method together with central space difference is known to be unconditionally unstable for pure advection problems. It is noteworthy that the Runge–Kutta central space discretization of the pure advection equation differs from the Lax–Wendroff one only in the approximation of the second derivative term. The former uses a larger computational stencil than the latter.

3.2.3. Implicit Euler method

For $\theta_c = 1$, Eq. (28) reduces to

$$f_\alpha^{n+1} - f_\alpha^n = -\Delta t\left[e_{\alpha r}\frac{\partial f_\alpha^n}{\partial x_r} + \frac{1}{\lambda}\left(f_\alpha - f_\alpha^{eq}\right)^{n+1}\right] + \frac{\Delta t^2}{2}e_{\alpha s}\frac{\partial}{\partial x_s}e_{\alpha r}\frac{\partial f_\alpha^n}{\partial x_r}. \tag{37}$$

Spatial gradients associated with the collision term disappear. This makes it attractive when direct discretization of the DBE is considered. The appropriate λ–ν relation for this scheme is $\lambda = \nu/c_s^2 - 0.5\Delta t$, i.e. Eq. (7) with $\theta_c = 1$.

In their finite difference LBE method, Mei and Shyy [3] evaluated the collision term at the t_{n+1} time level using the implicit Euler method and the second-order extrapolation of f_α^{eq} to enhance stability, while they treated the advection term using the explicit Euler method. $\lambda = \nu/c_s^2$ was used as in most of the DBE methods. The semi-discretized form of their method can be written as

$$f_\alpha^{n+1} - f_\alpha^n = -\Delta t\left[e_{\alpha r}\frac{\partial f_\alpha^n}{\partial x_r} + \frac{1}{\lambda}\left(f_\alpha - f_\alpha^{eq}\right)^{n+1}\right]. \tag{38}$$

The absence of the second derivative term in Eq. (38) makes the scheme only first-order accurate in time. The Chapman–Enskog analysis (see Appendix B) shows that Eq. (38) recovers the physically proper Navier–Stokes equations only at steady state because the first-order truncation error is time-dependent. At steady state, this time-dependent term disappears and consequently there is no such first-order term left that requires correction through modification of the λ–ν relation. Therefore, $\lambda = \nu/c_s^2$ might be a good choice for this first-order scheme. In general, not all the first-order schemes can recover the physically proper Navier–Stokes equations at steady state and the error caused by an inappropriate λ–ν relation becomes significant at high *Re* number and for large time step.

4. Implicit Taylor–Galerkin approximation

Among numerous discretization methods, we apply the implicit Taylor–Galerkin finite element method [8,9] to solve the pure advection equation (14). The finite element method permits geometric flexibility and the implicit scheme enables the use of large time step. The Taylor–Galerkin method is the Lax–Wendroff method [23] in the context of the finite element. Temporally second-order accurate Taylor–Galerkin approximation of the pure advection equation Eq. (14) starts from

$$\frac{\hat{f}_\alpha^{n+1} - \hat{f}_\alpha^n}{\Delta t} = -e_{\alpha r}\frac{\partial \hat{f}_\alpha^n}{\partial x_r} + \frac{\Delta t}{2}e_{\alpha s}\frac{\partial}{\partial x_s}\left[e_{\alpha r}\frac{\partial}{\partial x_r}\left(\theta_a\hat{f}_\alpha^{n+1} + (1-\theta_a)\hat{f}_\alpha^n\right)\right], \tag{39}$$

where the advection term is evaluated at the time t_n, while the second derivative terms can be evaluated anytime between t_n and t_{n+1}. Eq. (39) is unconditionally stable for $0.5 \leqslant \theta_a \leqslant 1$ and conditionally stable for $0 \leqslant \theta_a < 0.5$. As above, we call Eq. (39) *advection-explicit* (AE) scheme for $\theta_a = 0$ and *advection-implicit* (AI) scheme for $0 < \theta_a \leqslant 1$. While the CI scheme has no advantage over the CE scheme in terms of stability and time step, the AI scheme can indeed allow larger time step and is more stable than the AE scheme. Here we choose $\theta_a = 0.5$ for better phase and amplitude results as well as unconditional stability [8,9].

We now apply the standard Galerkin finite element method to Eq. (39). Suppose that the domain Ω is discretized into an appropriate collection of finite elements. The Galerkin approximation is to find an approximate solution of the following form in a finite dimensional subspace H^h of the Sobolev space on the spatial domain Ω.

$$\hat{f}_\alpha^{(h)} = \mathbf{N}^{\mathrm{T}} \hat{\mathbf{f}}_\alpha, \tag{40}$$

where $\mathbf{N}^{\mathrm{T}} = \{N^1, N^2, \ldots, N^{n_e}\}$ is a $(1 \times n_e)$ vector of interpolation functions of the element Ω^e, the superscript $(\cdot)^{\mathrm{T}}$ denotes the transpose operation, and n_e is the number of nodal points in an element. $\hat{\mathbf{f}}_\alpha$ is a $(n_e \times 1)$ vector of redefined nodal particle distribution functions.

Application of the Galerkin approximation to Eq. (39) with $\theta_a = 0.5$ yields

$$\mathbf{M}\left(\hat{\mathbf{f}}_\alpha^{n+1} - \hat{\mathbf{f}}_\alpha^{n}\right) = -\Delta t \mathbf{C}_\alpha \hat{\mathbf{f}}_\alpha^{n} + \frac{\Delta t^2}{2} \mathbf{D}_\alpha \left(\frac{\hat{\mathbf{f}}_\alpha^{n+1} + \hat{\mathbf{f}}_\alpha^{n}}{2} \right), \tag{41}$$

where $(n_e \times n_e)$ matrices $\mathbf{M}$, $\mathbf{C}_\alpha$, and $\mathbf{D}_\alpha$ are defined as

$$\mathbf{M} = \int_{\Omega^e} \mathbf{N}\mathbf{N}^{\mathrm{T}} \, \mathrm{d}\Omega, \tag{42}$$

$$\mathbf{C}_\alpha = \int_{\Omega^e} \mathbf{N} e_{\alpha \mathrm{r}} \frac{\partial \mathbf{N}^{\mathrm{T}}}{\partial x_{\mathrm{r}}} \, \mathrm{d}\Omega, \tag{43}$$

$$\mathbf{D}_\alpha = \int_{\Omega^e} \mathbf{N} e_{\alpha \mathrm{r}} e_{\alpha \mathrm{s}} \frac{\partial^2 \mathbf{N}^{\mathrm{T}}}{\partial x_{\mathrm{s}} \partial x_{\mathrm{r}}} \, \mathrm{d}\Omega. \tag{44}$$

The second derivative in Eq. (44) is integrated by parts and is converted by the divergence theorem of Gauss to

$$\mathbf{D}_\alpha = -\int_{\Omega^e} \frac{\partial \mathbf{N}}{\partial x_{\mathrm{s}}} e_{\alpha \mathrm{s}} e_{\alpha \mathrm{r}} \frac{\partial \mathbf{N}^{\mathrm{T}}}{\partial x_{\mathrm{r}}} \, \mathrm{d}\Omega + \int_{\Gamma^e} \mathbf{N} n_{\mathrm{s}} e_{\alpha \mathrm{s}} e_{\alpha \mathrm{r}} \frac{\partial \mathbf{N}^{\mathrm{T}}}{\partial x_{\mathrm{r}}} \, \mathrm{d}\Gamma, \tag{45}$$

where Γ^e denotes the surface of elements and n_s is the unit vector outward normal to Γ^e. The second term on the right-hand side is a surface integral and cancels out in the interior of the domain Ω.

The integrand of Eq. (45) requires evaluation of the spatial derivatives that are discontinuous across linear elements. To avoid evaluating the spatial derivatives, we replace the spatial derivatives with the time derivatives through the identity

$$\frac{\hat{f}_\alpha^{n+1} - \hat{f}_\alpha^{n}}{\Delta t} = -e_{\alpha \mathrm{r}} \frac{\partial}{\partial x_{\mathrm{r}}} \left(\frac{\hat{f}_\alpha^{n+1} + \hat{f}_\alpha^{n}}{2} \right) + \mathrm{O}(\Delta t^2). \tag{46}$$

The surface integral then takes the form

$$\int_{\Gamma^e} \mathbf{N} n_{\mathrm{s}} e_{\alpha \mathrm{s}} e_{\alpha \mathrm{r}} \frac{\partial \mathbf{N}^{\mathrm{T}}}{\partial x_{\mathrm{r}}} \left(\frac{\hat{\mathbf{f}}_\alpha^{n+1} + \hat{\mathbf{f}}_\alpha^{n}}{2} \right) \mathrm{d}\Gamma = -\int_{\Gamma^e} \mathbf{N} n_{\mathrm{s}} e_{\alpha \mathrm{s}} \mathbf{N}^{\mathrm{T}} \left(\frac{\hat{\mathbf{f}}_\alpha^{n+1} - \hat{\mathbf{f}}_\alpha^{n}}{\Delta t} \right) \mathrm{d}\Gamma + \mathrm{O}(\Delta t^2). \tag{47}$$

Eq. (41) now is recast as

$$\left(\mathbf{M}+\frac{\Delta t^2}{4}\tilde{\mathbf{D}}_\alpha-\frac{\Delta t}{2}\mathbf{S}_\alpha\right)\left(\hat{\mathbf{f}}_\alpha^{n+1}-\hat{\mathbf{f}}_\alpha^{n}\right)=-\Delta t\mathbf{C}_\alpha\hat{\mathbf{f}}_\alpha^{n}-\frac{\Delta t^2}{2}\tilde{\mathbf{D}}_\alpha\hat{\mathbf{f}}_\alpha^{n}, \tag{48}$$

where $(n_e \times n_e)$ matrix $\tilde{\mathbf{D}}_\alpha$ and (2×2) matrix $\mathbf{S}_\alpha$ are defined as

$$\tilde{\mathbf{D}}_\alpha=\int_{\Omega^e}\frac{\partial \mathbf{N}}{\partial x_s}e_{\alpha s}e_{\alpha r}\frac{\partial \mathbf{N}^T}{\partial x_r}\,d\Omega, \tag{49}$$

$$\mathbf{S}_\alpha=\int_{\Gamma^e}\mathbf{N}n_s e_{\alpha s}\mathbf{N}^T\,d\Gamma. \tag{50}$$

Since the matrices on the left-hand side of Eq. (48) is symmetric positive definite, it might be solved by the conjugate gradient (CG) solver using the solution from the previous time step as an initial guess. Up to this level, one-sided difference is applied to the boundary nodes, but it might render the solution unstable. Suppose that f_α and f_β represent particle distribution functions at domain boundaries with $\mathbf{e}_\alpha \cdot \mathbf{n} < 0$ and $\mathbf{e}_\beta \cdot \mathbf{n} > 0$. It is found that strong coupling between f_α and f_β through the boundary condition Eq. (17) greatly stabilizes the scheme. Without this boundary condition, f_α and f_β are weakly and indirectly coupled through macroscopic variables. Since f_α and f_β must be solved simultaneously to ensure strong coupling between them, we apply one-sided difference to f_β, and Eq. (17) to f_α which propagates into the domain. This makes the matrices on the left-hand side of Eq. (48) slightly asymmetric so that the CG solver is no longer applicable. We use the bi-conjugate gradient stabilized (BiCGSTAB) solver [24] instead. As Δt becomes smaller, the matrices on the left-hand side becomes closer to the well-conditioned mass matrix $\mathbf{M}$ and the BiCGSTAB solver converges with very small number of iterations. With larger Δt, the BiCGSTAB solver needs more iterations for convergence because of the additional diffusion matrix $\tilde{\mathbf{D}}_\alpha$ whose magnitude increases with Δt^2. The least squares finite element approximation [25] or the Galerkin finite element approximation with balancing tensor diffusivity/trapezoidal rule (BTD/TR) [26] of Eq. (14) also results in Eq. (48).

The boundary condition introduced above is quite general. For instance, the finite difference approach in conjunction with the one-sided difference and the above boundary condition for the boundary nodes can be easily implemented. Implementation of the implicit Lax–Wendroff type methods is summarized in [12].

5. Numerical test

Results of numerical experiments in this section are to illustrate three points. First, with the current formulation both the CE and CI schemes are equally stable and the AI scheme allows larger time step and enhances stability as compared with the AE scheme. Second, improper choice of the relaxation parameter changes the physical viscosity and thus, must be avoided. Third, the proposed boundary condition works well with the current formulation and is of second-order accuracy. We consider flow over a backward-facing step, lid-driven cavity flow, and steady and unsteady flow past a circular cylinder. All simulations presented here use $\theta_c = 0.5$ but any value of θ_c in [0,1] yields identical results. The *CFL* number in the following section is defined by

$$CFL=\frac{|\mathbf{e}_\alpha|\Delta t}{\Delta \mathbf{x}_{\min}}, \tag{51}$$

where $\Delta \mathbf{x}_{\min}$ is the minimum grid spacing in the direction of $\mathbf{e}_\alpha$.

5.1. Flow over a backward-facing step

The flow separation in the backward-facing step caused by the sudden change in geometry can be found in many applications. It serves to create a recirculation region or a sudden change in pressure. Here we consider laminar flow over a backward-facing step. The *Re* number based on mean inlet velocity and step height h ranges from 50 to 800. We will discuss the stability of different advection schemes and the effect of the relaxation parameter on the accuracy.

The computational domain for the simulation is shown in Fig. 1. The expansion number defined as the ratio of the main channel height to the step height is fixed at 2. The channel length is $30h$ and the inlet channel length is $5h$. The number of grid points is 11,075 and the total number of elements is 10,840. Due to sudden expansion and different velocity profiles at the inlet, predictions with inlet channel are usually different from those with no inlet channel. The *Ma* number based on the maximum inlet velocity is 0.15 and the initial density is given as $\rho = 1.0$. Eq. (17) is used as the boundary condition for both stationary walls and the inlet where parabolic velocity profile is prescribed. At the outflow boundary, the Neumann condition is imposed for velocities and one-sided difference is used for $\hat{f}_\alpha$.

Fig. 2 shows the maximum allowable *CFL* number of the AE/CI scheme and the RK2-DBE scheme of Cao et al. [2] at different *Re* numbers. $\theta_c = 0.5$ is used in the AE/CI scheme in order to compare with the RK2-DBE scheme. With this choice of the θ_c value, the relaxation parameter is given by $v = \lambda c_s^2$. In the low *Re* number regime ($Re < 100$), the maximum *CFL* number of the RK2-DBE scheme is then governed by the formal stability limit of the second-order Galerkin Runge–Kutta scheme for the pure advection equation, which is $1/\sqrt{3}$ [27]. As the *Re* number increases, the maximum allowable *CFL* number closely follows the trend predicted by Eq. (36). It is clear that very small time step must be used at higher *Re* number. If time step is too small, not only does it take much time for convergence but the solution is more likely to become oscillatory though more time-accurate [8]. It is because the effect of stabilization arising from the second derivatives, whose coefficient is proportional to Δt^2, diminishes with decreasing Δt. In contrast, the maximum allowable *CFL* number for the AE/CI scheme, which is also about $1/\sqrt{3}$ [9,28], is much greater than that of the RK2-DBE scheme especially at high *Re* number, and only slightly decreases with increasing *Re* number. The AI/CI scheme generally permits much larger *CFL* number than the AE/CI scheme in moderate *Re* number range. For very high *Re* number flows, small time step must be used anyway to resolve fine scale flow features.

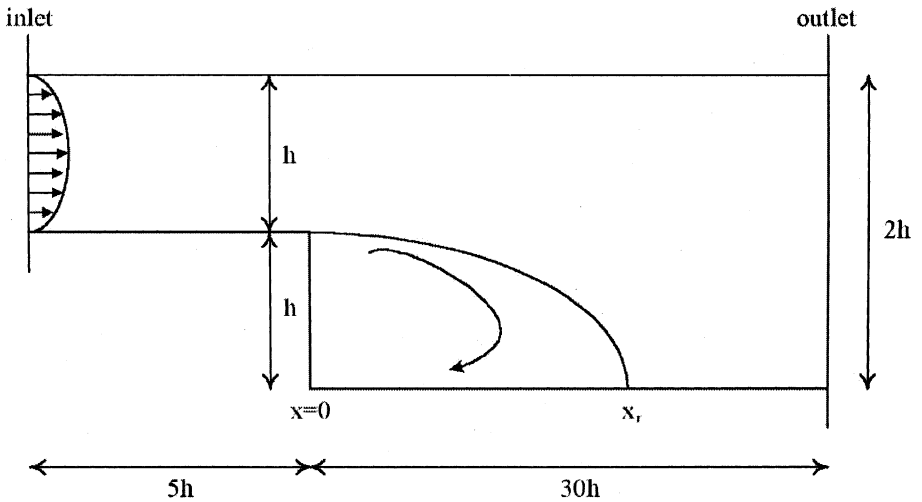

Fig. 1. Backward-facing step geometry (not to scale).

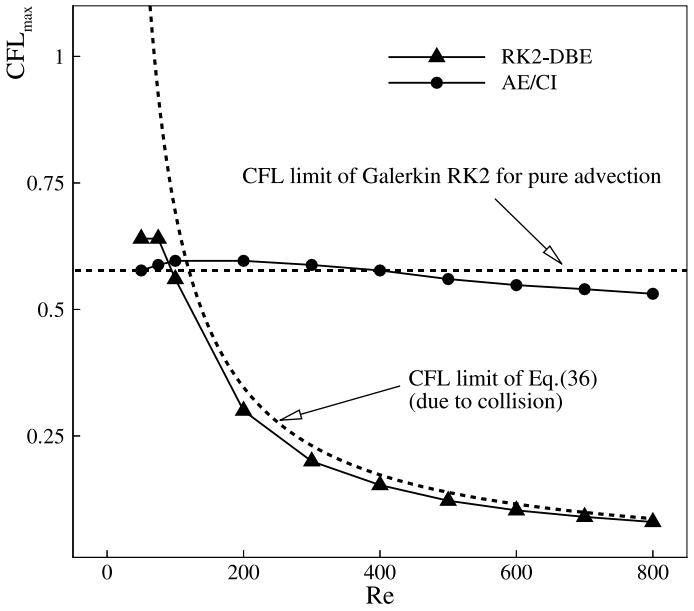

Fig. 2. Maximum allowable *CFL* number of RK2-DBE and AE/CI schemes with Reynolds number.

Next we shall examine the effect of the relaxation parameter on the accuracy of solution. Recall that satisfaction of Eq. (7) is a necessity to correctly recover the Navier–Stokes equations. For instance, use of $v = \lambda c_s^2$ requires $\theta_c = 0.5$. If the implicit Euler method is applied to the collision term ($\theta_c = 1$), the right form of the λ–v relation is $v = \lambda c_s^2 + 0.5 c_s^2 \Delta t$. If $v = \lambda c_s^2$ is still used, it will result in $O(\Delta t)$ error whose effect becomes significant as the *Re* number increases. Fig. 3 shows the reattachment length x_r as a function of the *Re* number. The relaxation parameter is calculated from $v = \lambda c_s^2$ for all cases, but different values of θ_c and *CFL* numbers are used. With this λ–v relation, the result for $\theta_c = 0.5$ and $CFL = 5$ agrees very well with the benchmark solution of Barton [29], but the results for $\theta_c = 1$ underpredict the length due to the relaxation parameter calculated from the incorrect λ–v relation. The difference becomes even more evident as the *Re* number increases. Since the error is of $O(\Delta t)$, the solutions become much less accurate with increasing *CFL* number as shown in Fig. 3.

5.2. Lid-driven cavity flow

The lid-driven cavity flow is considered to estimate the accuracy of the current scheme at moderately high *Re* number. The *Re* number is defined by the velocity and length of the top lid. The solutions are obtained using $Ma = 0.15$, and the initial density $\rho = 1.0$. In order to demonstrate the spatial accuracy, calculations are performed on three systematically refined uniform meshes (denoted by the subscripts $4h$, $2h$, and h) with $CFL = 1.0$. Since the ratio of the mesh size on successive meshes is 2, the order of the scheme, p, can be estimated from [30]

$$p = \frac{\ln\left(\frac{\phi_{2h} - \phi_{4h}}{\phi_h - \phi_{2h}}\right)}{\ln 2}, \tag{52}$$

which yields $p = 2.1$. This confirms the second-order accuracy of the scheme as well as the boundary condition.

To examine the effect of *CFL* number on the accuracy, we compare the results of $Re = 400$ and $Re = 5000$. 65×65 nonuniform mesh is used for both cases. Comparison of the profiles of the horizontal

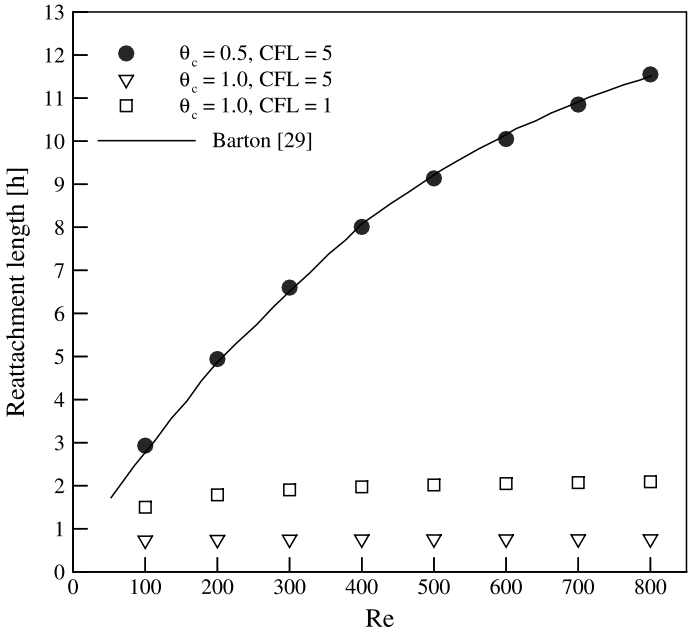

Fig. 3. Reattachment length with Reynolds number ($v = \lambda c_s^2$).

velocity component in the vertical symmetry plane is shown in Fig. 4. At $Re = 400$, large CFL number effect is not as apparent as at $Re = 5000$. For instance, the case with $CFL = 2$ yields nearly the same result as the cases with $CFL = 0.5$ and 1 at $Re = 400$ but slight deviation is observed at $Re = 5000$. With $CFL = 8$, the result at $Re = 400$ also shows some deviation from benchmark result. The simulation at $Re = 5000$ is unstable with $CFL = 8$ due to a large collision coefficient. The pressure contours and the streamlines at

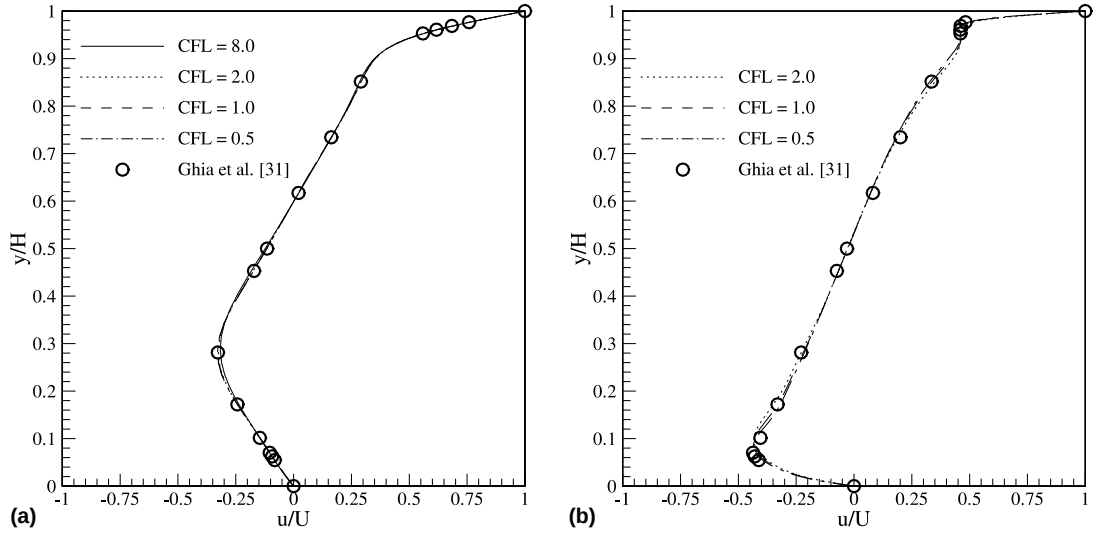

Fig. 4. Profiles of normalized velocity component u through the geometric center of the cavity at: (a) $Re = 400$ and (b) $Re = 5000$. (Ghia et al. [31]).

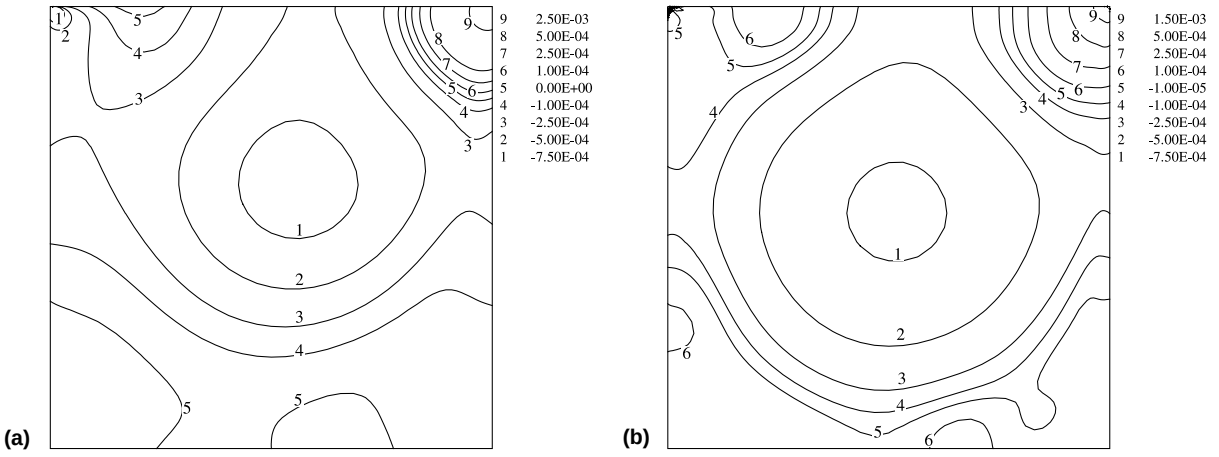

Fig. 5. Pressure contours of the cavity flow at: (a) $Re = 400$ and (b) $Re = 5000$.

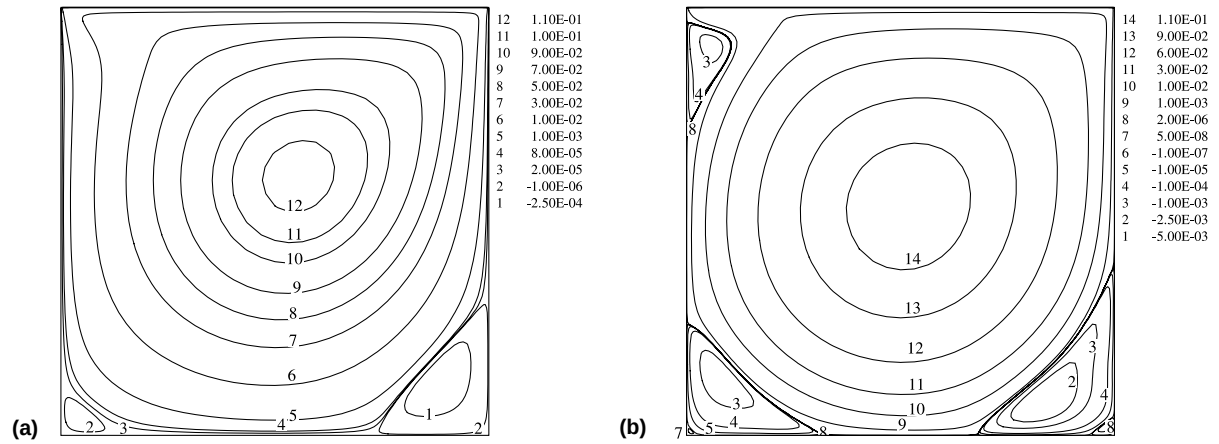

Fig. 6. Streamlines of the cavity flow at: (a) $Re = 400$ and (b) $Re = 5000$.

$Re = 400$ and 5000 with $CFL = 2$ are shown in Figs. 5 and 6, respectively. Comparison with those obtained from the conventional LBE method, e.g., Figs. 1 and 5 in [32], shows good agreement. Nevertheless the pressure contours in Fig. 5(e) of [32] exhibit oscillatory pattern although a 256×256 lattice is used. The appearance of this pattern is consistent with the discussion following Eq. (26) about the amplification factor approaching -1. Velocity vectors for $CFL = 2.0$ near singularities at upper corners are also shown in Fig. 7.

5.3. Flow past a circular cylinder

We consider laminar steady and unsteady flow past a circular cylinder on unstructured mesh. Figs. 8 and 9 show an unstructured hybrid mesh setup with $r_0 = 0.5$, which is the same for all the cases. Bi-linear quadrilateral elements are used near the cylinder wall, and linear triangular elements are used elsewhere. It is because quadrilateral elements are better suited for boundary-layer type flow and triangular elements are more favorable for mesh clustering and coarsening. The number of grid points on the cylinder wall is 128

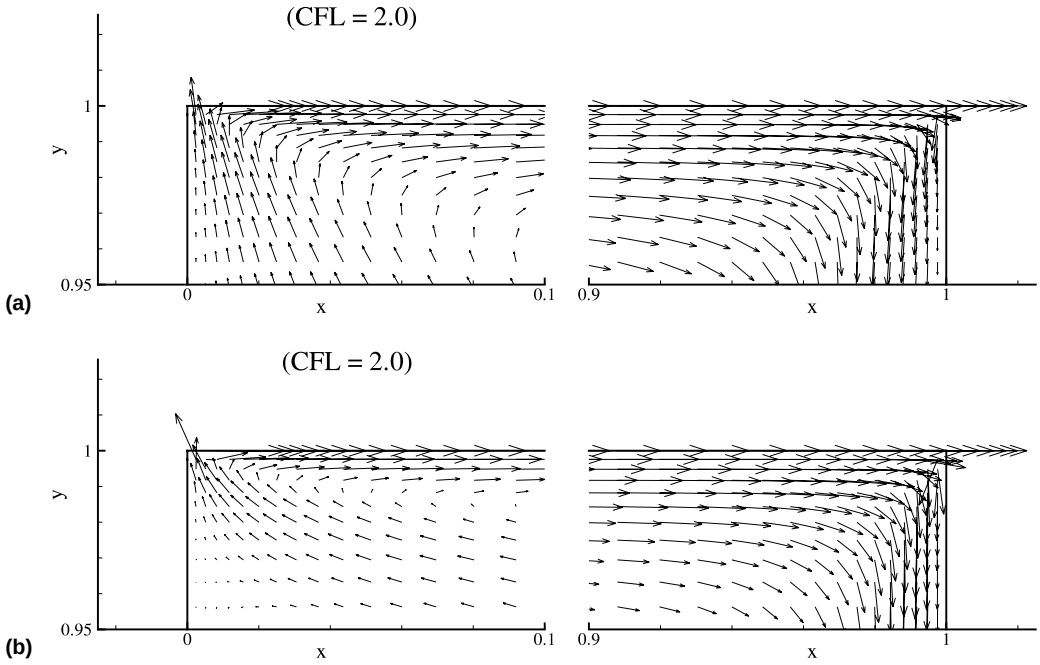

Fig. 7. Velocity vectors near singularities at the upper left and right corners at: (a) $Re = 400$ and (b) $Re = 5000$.

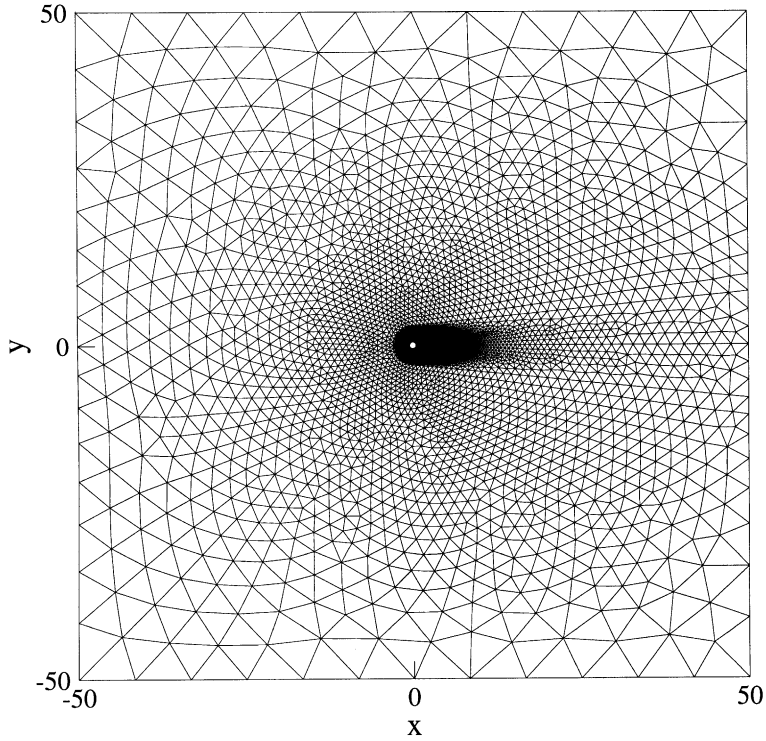

Fig. 8. Hybrid unstructured mesh (far view).

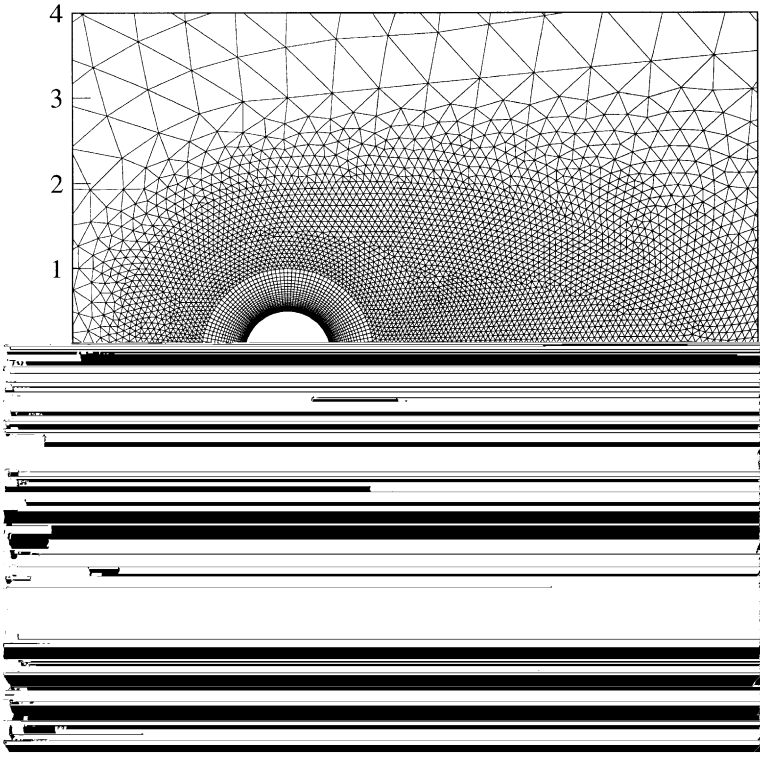

Fig. 9. Hybrid unstructured mesh (close view).

and the total number of grid points and elements are 12,726 and 22,190, respectively. Also, the *Ma* number based on the inlet velocity is 0.1.

5.3.1. Low Reynolds number flow

Here, $Re = 20$ and $Re = 100$ are considered in the simulation in order to show how *AI* scheme can increase time step and enhance stability. A uniform velocity $\mathbf{u} = (u_\infty, 0)$ is specified along the domain perimeter as physical boundary conditions and zero velocities are imposed at the cylinder surface. The Stokes solution is used as initial velocities and $\rho = 1.0$ is used for an initial density.

Five cases with the same physical configuration but different *CFL* numbers 0.5, 1, 10, 50, and 100 are tested. At $CFL = 0.5$, the AE/CI scheme rather than the AI/CI scheme is used for comparison. The *CFL* condition of the AE/CI scheme is given as $CFL \leqslant 1/\sqrt{3}$ [9,28]. Again, the treatment of the collision term shows no effect on the result.

Flow behind a circular cylinder remains symmetric up to $Re = (2u_\infty r_0)/v \approx 40$, where u_∞ is the free stream velocity and r_0 is the cylinder radius. At the *Re* number of 20, steady recirculation bubbles are attached to the cylinder surface. From Table 1 we can compare quantitatively the wake length ($L/2r_0$) and the drag coefficient (C_D) obtained by the current scheme with some benchmark data. The drag coefficient is calculated by

$$C_D = \frac{1}{\rho u_\infty^2 r_0} \int \mathbf{S} \cdot \mathbf{n} \, d\Gamma, \tag{53}$$

where $\mathbf{n}$ is the outward normal vector on the cylinder wall and

Table 1
Comparison of the wake length and the drag coefficient for flow past a circular cylinder at $Re = 20$

Authors	$L/2r_0$	C_D
Nieuwstadt and Keller[a] (1973)	1.786	2.053
Fornberg[b] (1980)	1.82	2.000
He and Doolen[c] (1997)	1.842	2.152
Mei and Shyy[d] (1997)	1.804	–
Present AE/CI ($CFL = 0.5$)[e]	1.849	2.086
Present AI/CI ($CFL = 1$)[e]	1.834	2.106
Present AI/CI ($CFL = 10$)[e]	1.844	2.092
Present AI/CI ($CFL = 50$)[e]	1.786	2.109
Present AI/CI ($CFL = 100$)[e]	1.746	2.052

[a] Numerical simulation of Navier–Stokes equations [33].
[b] Numerical simulation of Navier–Stokes equations [34].
[c] ISLBE with 181×241 grid points [21].
[d] FDLBM with 129×64 grid points [3].
[e] Unstructured mesh with 12,726 grid points.

$$\mathbf{S} = -p\mathbf{I} + \rho\nu\left(\nabla\mathbf{u} + (\nabla\mathbf{u})^{\mathrm{T}}\right) \tag{54}$$

is the stress tensor and $\mathbf{I}$ is an identify matrix. As shown in Table 1, the wake length and the drag coefficient at large CFL numbers are in good agreement with those of the previous studies although the wake length at $CFL = 100$ is slightly underpredicted (about 5.6% less than that of the $CFL = 0.5$ case).

The CPU time required for convergence on the HP 9000/785 workstation is presented in Table 2. It is the time when the number of time steps $\times$ the CFL number reaches 50,000. The diagonal preconditioner is used for the cases of $CFL = 0.5$ and 1, while the SSOR preconditioner [35] is used for the cases of $CFL = 10$, 50, and 100. The SSOR preconditioner works better for high CFL number cases. No special optimization is performed but substantial speedup (a factor of about 20) is observed as the CFL number increases. The speedup is not a linear function of the CFL number because the BiCGSTAB solver requires more iterations per time step with larger Δt. Fig. 10 displays the streamlines and the contours of pressure and vorticity for the $CFL = 50$ case. A pair of stationary recirculating bubbles develops behind the cylinder, being similar to Fig. 3 in [21].

At $Re = 100$, unsteady vortex shedding occurs behind the cylinder. The Strouhal (St) frequency and the maximum drag and lift coefficients at $CFL = 1$ and 10 are displayed in Table 3. They are in good agreement with the data obtained by Beaudan [36]. The difference between maximum C_D (C_L) values for $CFL = 1$ and 10 is only about 1.5% (3%). Fig. 11 displays the streamlines and the contours of pressure and vorticity for the $CFL = 10$ case. It should be cautioned that temporal truncation errors increase with time step so that it is not recommended to use too large time step for unsteady problems from the sake of accuracy.

Table 2
CPU time for convergence for flow past a circular cylinder at $Re = 20$

Schemes (CFL number)	CPU time (s)[a]	Speedup[b]	$\Delta t/\lambda$
AE/CI ($CFL = 0.5$)	37,393	1.0	0.33
AI/CI ($CFL = 1$)	16,523	2.3	0.65
AI/CI ($CFL = 10$)	2427	15.4	6.52
AI/CI ($CFL = 50$)	2104	17.8	32.62
AI/CI ($CFL = 100$)	1744	21.4	65.24

[a] CPU time required for convergence.
[b] Speedup over AE/CI scheme with $CFL = 0.5$.

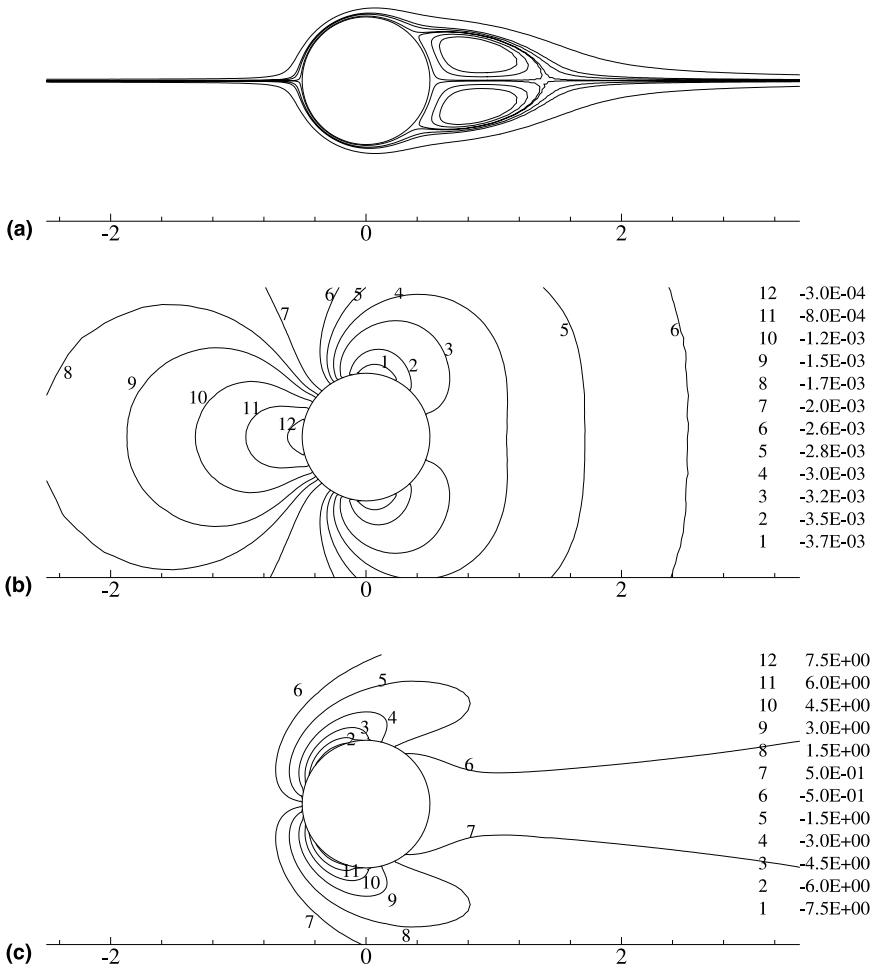

Fig. 10. (a) Streamlines, (b) pressure contours, and (c) vorticity contours obtained from the AI/CI scheme at $Re = 20$ and $CFL = 50$.

Table 3
Computed Strouhal number and lift and drag maxima at $Re = 100$

Author (*CFL* number)	*St*	max C_L	max C_D
Present AI/CI ($CFL = 1$)	0.1639	0.331	1.358
Present AI/CI ($CFL = 10$)	0.1632	0.321	1.338
Beaudan [36]	0.164	0.342	1.365

5.3.2. *Impulsively started high Reynolds number flow*

As demonstrated in the previous vortex shedding case, a large time step or a large *CFL* number deteriorates solution accuracy because the present scheme is of second-order accuracy in time. The degradation of solution accuracy would manifest itself more significantly for time dependent problems. Therefore, it is worth examining the solution accuracy at high Reynolds number with large time step for time dependent flows. We study flow past a circular cylinder impulsively started from rest and observe flow patterns and solution accuracy at different times expressed in units of r_0/u_∞. Boundary conditions are the same as above.

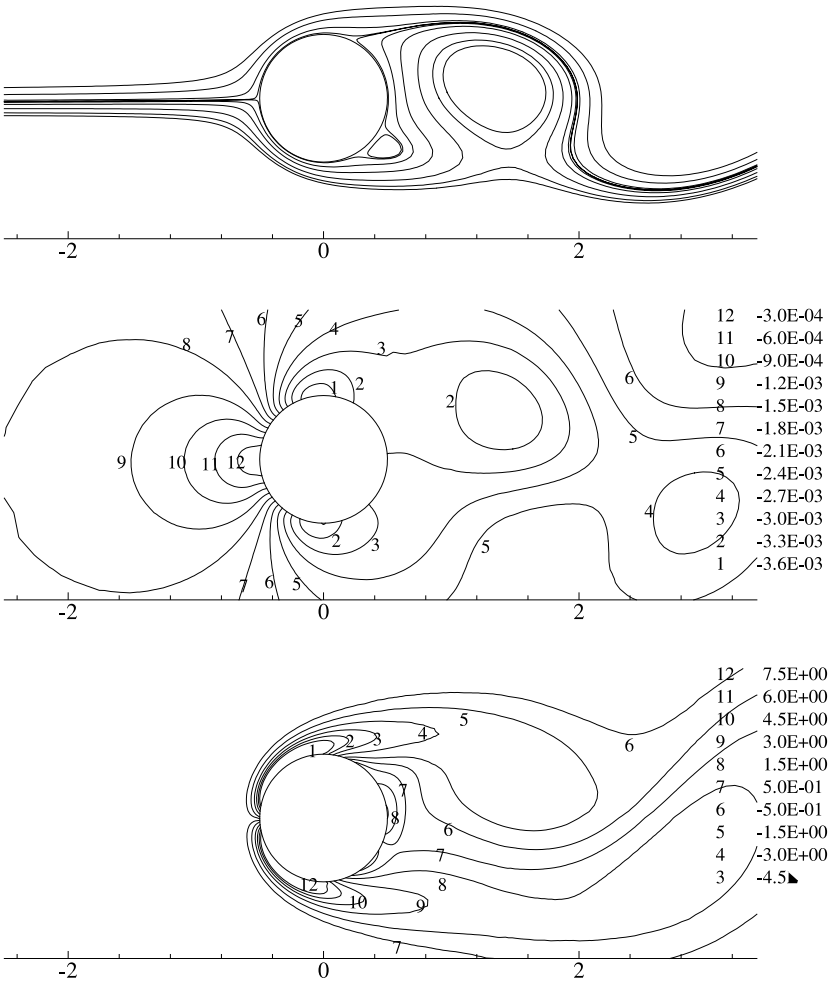

Typical flow patterns at $Re = 550$ are described as the bulge phenomenon and isolated secondary eddy [37]. First, near the wall and half-way between the stagnation and the separation points, the streamline deviate from the cylinder wall causing a bulge. This bulge then evolves into a closed secondary eddy, wh rotates in the opposite direction to the main eddy. Flow at $Re = 3000$ is typified by the so-calle nomenon α [37]. When the secondary eddy is fully developed, its boundary touches the bounda main recirculating zone. This splits the main eddy into two parts and isolates the region of the w the separation point. Finally, another secondary eddy is formed.

Time evolutions of the streamlines are shown in Fig. 12 for $Re = 550$ and Fig. 13 for R plot, upper (lower) half shows small (large) time step case with $CFL = 0.2$ (2.0). The higher CFL number case grows faster than that of the lower CFL number case and t more evident at higher Re number. The bulge phenomenon and isolated seconda in Figs. 12(a) and (b), respectively. Phenomenon α is also observed in Fig. 13. T lengths with different CFL numbers are compared with experimental [37].

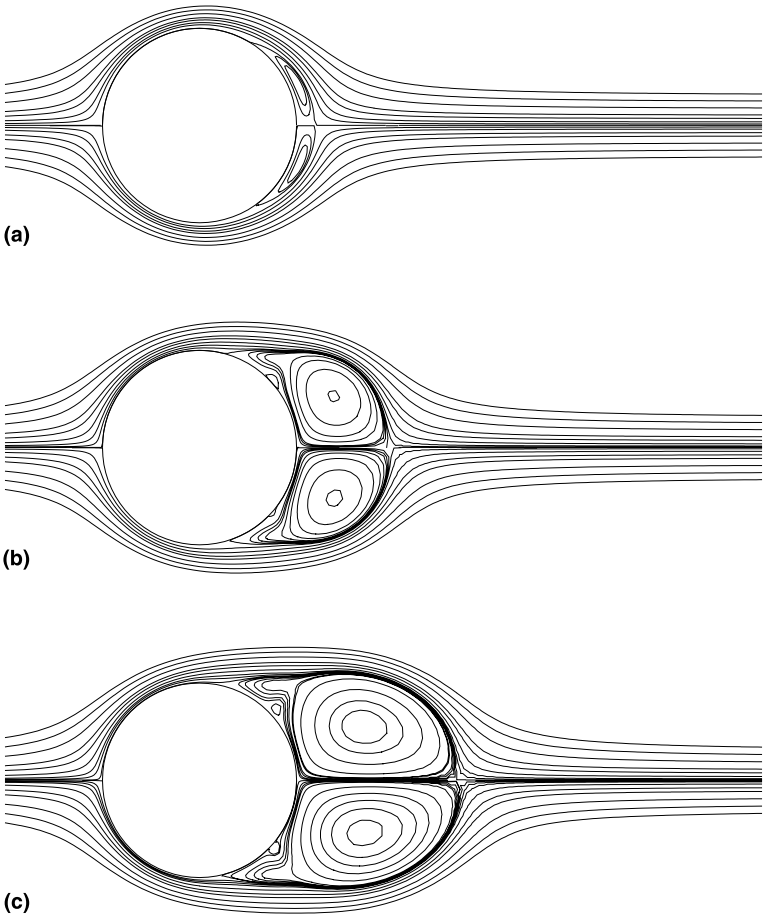

Fig. 12. Time evolutions of streamlines at $Re = 550$ for $CFL = 0.2$ and $CFL = 2.0$. (a) $t = 1$, $CFL = 0.2$ (upper half), $CFL = 2.0$ (lower half); (b) $t = 3$, $CFL = 0.2$ (upper half), $CFL = 2.0$ (lower half); (c) $t = 5$, $CFL = 0.2$ (upper half), $CFL = 2.0$ (lower half).

Fig. 14. At $Re = 550$, all cases agree well with the experimental data. With $Re = 3000$, only the case with small $CFL = 0.2$ accurately predicts initial wake lengths. The number of grid points in the present cases is 12,726, whereas that of [21] shown in Fig. 14 is 58,081 (241×241).

6. Concluding remarks

In the paper, we derived the LBE by discretizing the DBE along characteristics. The LBE possesses two appealing features. One is a local nature of the collision step. It permits easy treatment of the collision term in either explicit or implicit way if the relationship between the relaxation time and the kinematic viscosity is properly described. The other feature is that the streaming can be viewed as solving a pure advection equation in an Eulerian framework. By recognizing this point, virtually any second-order accurate scheme for solving the pure advection equation on either structured or unstructured mesh can be used to substitute the perfect shift (or streaming) on uniform lattice. Compared with other DBE methods, this approach is much more stable, allowing large time step. In this paper, we considered the Lax–Wendroff type advection

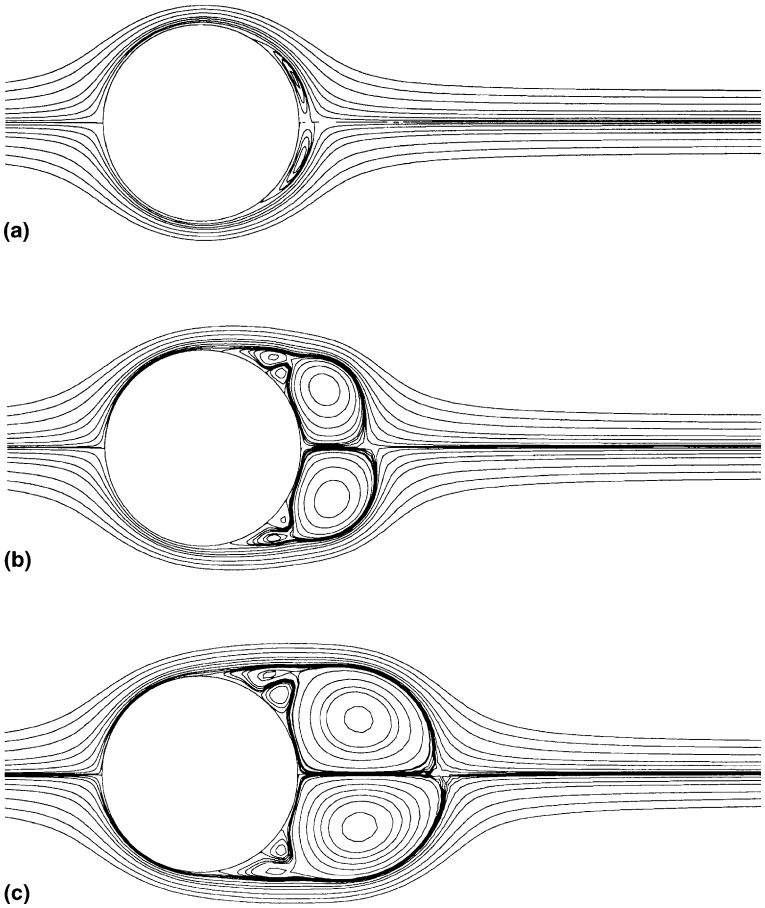

Fig. 13. Time evolutions of streamlines at $Re = 3000$ for $CFL = 0.2$ and $CFL = 2.0$. (a) $t = 1$, $CFL = 0.2$ (upper half), $CFL = 2.0$ (lower half); (b) $t = 3$, $CFL = 0.2$ (upper half), $CFL = 2.0$ (lower half); (c) $t = 5$, $CFL = 0.2$ (upper half), $CFL = 2.0$ (lower half).

scheme and showed that it leads to the proper Navier–Stokes equations through the Chapman–Enskog expansion when combined with the collision step.

We conducted several test cases, including flow over a backward-facing step, lid-driven cavity flow, and flow past a circular cylinder. From the results of flow over a backward-facing step with different time stepping methods for the collision term and different *CFL* numbers, we confirmed that the use of the relaxation parameter consistent with the time stepping method is indeed crucial. Improper choice of the relaxation parameter would result in overly diffusive solutions. By examining lid-driven cavity flow at different *Re* numbers with various *CFL* numbers, we found that large time step could affect accuracy of solution and stability of the scheme for high *Re* number flow. Five different *CFL* numbers (0.5, 1, 10, 50, and 100) were used for comparison of convergence rate and accuracy of flow past a circular cylinder at low *Re* number. The new scheme was found to improve significantly the convergence rate by a factor of more than 20 with reasonable accuracy. Impulsively started flows past a circular cylinder at moderate and high *Re* numbers were also investigated. Accuracy for transient flows is much more sensitive to time step than that for steady flows.

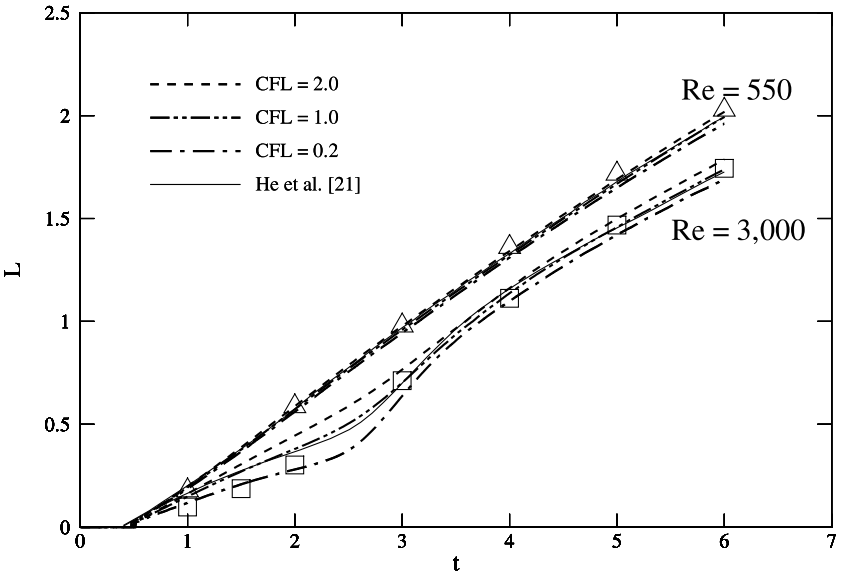

Fig. 14. Time evolutions of the wake lengths at $Re = 550$ and $Re = 3000$ for $CFL = 0.2$, 1.0, and 2.0. The experimental data [37] are denoted by triangle and square symbols.

Acknowledgements

This work was supported by the Carver Scientific Research Initiative Grants Program at the University of Iowa. The partial support of the IIHR – Hydroscience and Engineering at the University of Iowa is also acknowledged.

Appendix A

The Chapman–Enskog expansion of the second-order time accurate scheme Eq. (28) is considered to identify the kinematic viscosity given in Eq. (25) [32]. Eq. (28) is rearranged to give

$$f_\alpha^{n+1} - f_\alpha^n + \Delta t e_{\alpha r}\frac{\partial f_\alpha^n}{\partial x_r} - \frac{\Delta t^2}{2} e_{\alpha s}\frac{\partial}{\partial x_s} e_{\alpha r}\frac{\partial f_\alpha^n}{\partial x_r} = -\frac{(1-\theta_c)}{\tau}\left[1 - \Delta t e_{\alpha r}\frac{\partial}{\partial x_r} + \frac{\Delta t^2}{2} e_{\alpha s}\frac{\partial}{\partial x_s} e_{\alpha r}\frac{\partial}{\partial x_r}\right]\left(f_\alpha - f_\alpha^{eq}\right)^n - \frac{\theta_c}{\tau}\left(f_\alpha - f_\alpha^{eq}\right)^{n+1} + O(\Delta t^3), \tag{A.1}$$

where $\tau = \lambda/\Delta t$. If all variables of Eq. (A.1) are defined at $\tilde{\mathbf{x}} + \Delta t\mathbf{e}_\alpha$, Eq. (A.1) is rewritten in vector form as follows.

$$\begin{aligned} &f_\alpha(\tilde{\mathbf{x}} + \Delta t\mathbf{e}_\alpha, t + \Delta t) - f_\alpha(\tilde{\mathbf{x}} + \Delta t\mathbf{e}_\alpha, t) + \Delta t(\mathbf{e}_\alpha \cdot \nabla) f_\alpha(\tilde{\mathbf{x}} + \Delta t\mathbf{e}_\alpha, t) - \frac{\Delta t^2}{2}(\mathbf{e}_\alpha \cdot \nabla)^2 f_\alpha(\tilde{\mathbf{x}} + \Delta t\mathbf{e}_\alpha, t) \\ &= -\frac{(1-\theta_c)}{\tau}\left(f_\alpha - f_\alpha^{eq}\right)\Big|_{(\tilde{\mathbf{x}},t)} - \frac{\theta_c}{\tau}\left(f_\alpha - f_\alpha^{eq}\right)\Big|_{(\tilde{\mathbf{x}}+\Delta t\mathbf{e}_\alpha, t+\Delta t)} + O(\Delta t^3) \\ &= -\frac{1}{\tau}\left(f_\alpha - f_\alpha^{eq}\right)\Big|_{(\tilde{\mathbf{x}}+\theta_c\Delta t\mathbf{e}_\alpha, t+\theta_c\Delta t)} + O(\Delta t^3). \end{aligned} \tag{A.2}$$

Taylor-series expansion of Eq. (A.2) around $(\tilde{\mathbf{x}} + \theta_c \Delta t \mathbf{e}_\alpha, t + \theta_c \Delta t)$ at which the collision term is defined is required for analysis. For reference,

$$f_\alpha(\tilde{\mathbf{x}} + \Delta t \mathbf{e}_\alpha, t + \Delta t) = f_\alpha(\tilde{\mathbf{x}} + \theta_c \Delta t \mathbf{e}_\alpha, t + \theta_c \Delta t) + (1 - \theta_c)\Delta t \left[\frac{\partial}{\partial t} + (\mathbf{e}_\alpha \cdot \nabla)\right] f_\alpha(\tilde{\mathbf{x}} + \theta_c \Delta t \mathbf{e}_\alpha, t + \theta_c \Delta t) + \frac{(1 - \theta_c)^2 \Delta t^2}{2} \left[\frac{\partial}{\partial t} + (\mathbf{e}_\alpha \cdot \nabla)\right]^2 f_\alpha(\tilde{\mathbf{x}} + \theta_c \Delta t \mathbf{e}_\alpha, t + \theta_c \Delta t) + \mathrm{O}(\Delta t^3), \tag{A.3}$$

and

$$f_\alpha(\tilde{\mathbf{x}} + \Delta t \mathbf{e}_\alpha, t) = f_\alpha(\tilde{\mathbf{x}} + \theta_c \Delta t \mathbf{e}_\alpha, t + \theta_c \Delta t) - \Delta t \left[\theta_c \frac{\partial}{\partial t} - (1 - \theta_c)(\mathbf{e}_\alpha \cdot \nabla)\right] f_\alpha(\tilde{\mathbf{x}} + \theta_c \Delta t \mathbf{e}_\alpha, t + \theta_c \Delta t) + \frac{\Delta t^2}{2} \left[\theta_c \frac{\partial}{\partial t} - (1 - \theta_c)(\mathbf{e}_\alpha \cdot \nabla)\right]^2 f_\alpha(\tilde{\mathbf{x}}. + \theta_c \Delta t \mathbf{e}_\alpha, t + \theta_c \Delta t) + \mathrm{O}(\Delta t^3). \tag{A.4}$$

Substituting Eq. (A.2) with the above relations and retaining terms up to $\mathrm{O}(\Delta t^2)$ result in

$$\Delta t \left[\frac{\partial}{\partial t} + (\mathbf{e}_\alpha \cdot \nabla)\right] f_\alpha + (1 - 2\theta_c) \frac{\Delta t^2}{2} \left[\frac{\partial}{\partial t} + (\mathbf{e}_\alpha \cdot \nabla)\right]^2 f_\alpha = -\frac{1}{\tau}\left(f_\alpha - f_\alpha^{\mathrm{eq}}\right). \tag{A.5}$$

Identical result is obtained if we begin with the LBE Eq. (6) instead of Eq. (A.1) for expansion. If $\theta_c = 0.5$, Eq. (A.5) becomes the DBE Eq. (1) up to second-order accuracy. As shown below, for any other value of $\theta_c \in [0, 1]$, Eq. (A.5) can still generate a second-order accurate solution by choosing an appropriate τ value.

We consider the long-wavelength and low-frequency limits such that Δt can be regarded as small parameters compared with the macroscopic characteristic scales. It leads to the following relations

$$\frac{\partial}{\partial t} = \frac{\partial}{\partial t_0} + \Delta t \frac{\partial}{\partial t_1} + \cdots \tag{A.6}$$

and

$$f_\alpha = f_\alpha^{\mathrm{eq}} + \Delta t f_\alpha^{(1)} + \Delta t^2 f_\alpha^{(2)} + \cdots. \tag{A.7}$$

We obtain the equation to the order of Δt by substituting Eqs. (A.6) and (A.7) into Eq. (A.5)

$$\left[\frac{\partial}{\partial t_0} + (\mathbf{e}_\alpha \cdot \nabla)\right] f_\alpha^{\mathrm{eq}} = -\frac{1}{\tau} f_\alpha^{(1)}, \tag{A.8}$$

and the equation of order Δt^2

$$\frac{\partial f_\alpha^{\mathrm{eq}}}{\partial t_1} + \left[\frac{\partial}{\partial t_0} + (\mathbf{e}_\alpha \cdot \nabla)\right] \left(\frac{2\tau - 1 + 2\theta_c}{2\tau}\right) f_\alpha^{(1)} = -\frac{1}{\tau} f_\alpha^{(2)}. \tag{A.9}$$

The hydrodynamic quantities of fluid density $\rho(\mathbf{x}, t)$ and velocities $\mathbf{u}(\mathbf{x}, t)$ are defined as

$$\begin{aligned} \rho &= \sum_\alpha f_\alpha^{\mathrm{eq}}, \\ \rho \mathbf{u} &= \sum_\alpha \mathbf{e}_\alpha f_\alpha^{\mathrm{eq}}. \end{aligned} \tag{A.10}$$

After some algebraic manipulation, we finally obtain the governing equations.

$$\frac{\partial \rho}{\partial t} + \nabla \cdot \rho \mathbf{u} = 0, \tag{A.11}$$

$$\frac{\partial(\rho\mathbf{u})}{\partial t} + \nabla\cdot\left(\Pi^{(0)} + \Pi^{(1)}\right) = 0, \tag{A.12}$$

where the momentum flux tensors are defined by

$$\begin{aligned}\Pi^{(0)} &= \sum_{\alpha}\mathbf{e}_{\alpha}\mathbf{e}_{\alpha}f_{\alpha}^{\mathrm{eq}} = p\mathbf{I} + \rho\mathbf{u}\mathbf{u},\\ \Pi^{(1)} &= \left(\frac{2\tau - 1 + 2\theta_{\mathrm{c}}}{2\tau}\right)\sum_{\alpha}\mathbf{e}_{\alpha}\mathbf{e}_{\alpha}f_{\alpha}^{(1)} = \frac{v}{\Delta t}\rho[\nabla_{\mathrm{r}}u_{\mathrm{s}} + \nabla_{\mathrm{s}}u_{\mathrm{r}}],\end{aligned} \tag{A.13}$$

where $p = c_{\mathrm{s}}\rho$ is the pressure and $v = (\tau - 0.5 + \theta_{\mathrm{c}})c_{\mathrm{s}}^2\Delta t$ is the kinematic viscosity. The macroscopic equations are

$$\begin{aligned}&\frac{\partial\rho}{\partial t} + \nabla\cdot\rho\mathbf{u} = 0,\\ &\rho\left[\frac{\partial\mathbf{u}}{\partial t} + \mathbf{u}\cdot\nabla\mathbf{u}\right] = -\nabla p + [\nabla\cdot(\rho v\nabla\mathbf{u}) + \nabla\rho v\nabla\cdot\mathbf{u}].\end{aligned} \tag{A.14}$$

Nonzero θ_{a} will lead to the same result because it acts as a third-order correction.

Appendix B

The Chapman–Enskog expansion of the first-order time accurate scheme Eq. (38) is considered to identify the first-order truncation error term. Eq. (38) is shown again for reference.

$$f_{\alpha}^{n+1} - f_{\alpha}^{n} + \Delta t e_{\alpha\mathrm{r}}\frac{\partial f_{\alpha}^{n}}{\partial x_{\mathrm{r}}} = -\frac{1}{\tau}\left(f_{\alpha} - f_{\alpha}^{\mathrm{eq}}\right)^{n+1}. \tag{B.1}$$

The same procedure used in Appendix A leads to

$$\Delta t\left[\frac{\partial}{\partial t} + (\mathbf{e}_{\alpha}\cdot\nabla)\right]f_{\alpha} - \frac{\Delta t^2}{2}\left[\frac{\partial^2}{\partial t^2} + 2\frac{\partial}{\partial t}(\mathbf{e}_{\alpha}\cdot\nabla)\right]f_{\alpha} = -\frac{1}{\tau}\left(f_{\alpha} - f_{\alpha}^{\mathrm{eq}}\right). \tag{B.2}$$

The second derivative term in Eq. (B.2) looks different from the correct form in Eq. (A.5). Thus this scheme is only first-order accurate in time. Rearranging the arithmetic operators in the second square bracket yields

$$\Delta t\left[\frac{\partial}{\partial t} + (\mathbf{e}_{\alpha}\cdot\nabla)\right]f_{\alpha} - \frac{\Delta t^2}{2}\left[\frac{\partial}{\partial t} + 2(\mathbf{e}_{\alpha}\cdot\nabla)\right]\frac{\partial f_{\alpha}}{\partial t}$$

In Eq. (B.1), the explicit Euler method is applied to the advection term. One might be interested in the implicit Euler method for large time step. The implicit Euler method results in

$$\Delta t\left[\frac{\partial}{\partial t}+(\mathbf{e}_\alpha\cdot\mathbf{V})\right]f_\alpha-\frac{\Delta t^2}{2}\frac{\partial}{\partial t}\frac{\partial f_\alpha}{\partial t}=-\frac{1}{\tau}\left(f_\alpha-f_\alpha^{\mathrm{eq}}\right), \tag{B.5}$$

which also reduces to Eq. (B.4) at steady state. The rest of the analysis is identical to that of Appendix A.

References

[1] S. Chen, G.D. Doolen, Lattice Boltzmann method for fluid flows, Annu. Rev. Fluid Mech. 30 (1998) 329.
[2] N. Cao, S. Chen, S. Jin, D. Martínez, Physical symmetry and lattice symmetry in the lattice Boltzmann method, Phys. Rev. E 55 (1997) R21.
[3] R. Mei, W. Shyy, On the finite difference-based lattice Boltzmann method in curvilinear coordinates, J. Comput. Phys. 143 (1998) 426.
[4] H. Xi, G. Peng, S.-H. Chou, Finite-volume lattice Boltzmann method, Phys. Rev. E 59 (1999) 6202.
[5] H. Xi, G. Peng, S.-H. Chou, Finite-volume lattice Boltzmann schemes in two and three dimensions, Phys. Rev. E 60 (1999) 3380.
[6] T. Lee, C.-L. Lin, A characteristic Galerkin method for discrete Boltzmann equation, J. Comput. Phys. 171 (2001) 1.
[7] D. Wolf-Gladrow, Lattice-Gas Cellular Automata and Lattice Boltzmann Models, Springer, Heidelberg, 2000.
[8] O.C. Zienkiewicz, R. Taylor, Finite Element Method, vol. II, fourth ed., McGraw-Hill, New York, 1991.
[9] G. Comini, M. Manzan, C. Nonino, Analysis of finite element schemes for convection-type problems, Int. J. Numer. Methods Fluids 20 (1995) 443.
[10] P.L. Bhatnagar, E.P. Gross, M. Krook, A model for collision processes in gases. I. Small amplitude processes in charged and neutral one-component system, Phys. Rev. 94 (1954) 511.
[11] X. He, L.-S. Luo, A priori derivation of the lattice Boltzmann equation, Phys. Rev. E 55 (1997) R6333.
[12] C. Hirsch, Numerical Computation of Internal and External Flows, vol. II, Wiley, New York, 1990.
[13] X. He, X. Shan, G.D. Doolen, Discrete Boltzmann equation model for nonideal gases, Phys. Rev. E 57 (1998) R13.
[14] S. He, S. Chen, G.D. Doolen, A novel thermal model for the lattice Boltzmann method in incompressible limit, J. Comput. Phys. 146 (1998) 282.
[15] X. He, L.-S. Luo, Lattice Boltzmann model for the incompressible Navier–Stokes equation, J. Stat. Phys. 88 (1997) 927.
[16] J.D. Sterling, S. Chen, Stability analysis of lattice Boltzmann methods, J. Comput. Phys. 123 (1996) 196.
[17] J.H. Ferziger, Numerical Methods for Engineering Applications, Wiley–Interscience, New York, 1981.
[18] G.R. McNamara, A.L. Garcia, B.J. Alder, Stabilization of thermal lattice Boltzmann models, J. Stat. Phys. 81 (1995) 395.
[19] R. Zhang, H. Chen, Y.H. Qian, S. Chen, Effective volumetric lattice Boltzmann scheme, Phys. Rev. E 63 (2001) 056705.
[20] X. He, L.-S. Luo, M. Dembo, Some progress in lattice Boltzmann method. Part I. Nonuniform mesh grids, J. Comput. Phys. 129 (1996) 357.
[21] X. He, G.D. Doolen, Lattice Boltzmann method on curvilinear coordinates system: flow around a circular cylinder, J. Comput. Phys. 134 (1997) 306.
[22] S. Teng, Y. Chen, H. Ohashi, Lattice Boltzmann simulation of multiphase fluid flows through the total variation diminishing with artificial compression scheme, Int. J. Heat and Fluid Flow 21 (2000) 112.
[23] P.D. Lax, B. Wendroff, Systems of conservation laws, Comm. Pure Appl. Math. 13 (1960) 217.
[24] H.A. van der Vorst, Bi-CGSTAB: a fast and smoothly converging variant of Bi-CG for the solution of nonsymmetric linear systems, SIAM J. Sci. Stat. Comput. 13 (2) (1992) 631.
[25] B.N. Jiang, The Least-Squares Finite Element Method: Theory and Applications in Computational Fluid Dynamics and Electromagnetics, Springer, New York, 1998.
[26] P.M. Gresho, R.L. Sani, Incompressible Flow and the Finite Element Method, Wiley, New York, 1998.
[27] C.B. Jiang, M. Kawahara, The analysis of unsteady incompressible flows by a three-step finite element method, Int. J. Numer. Methods Fluids 16 (1993) 793.
[28] O.C. Zienkiewicz, R. Codina, A general algorithm for compressible and incompressible flow – part I. The split, characteristic-based scheme, Int. J. Numer. Methods Fluids 20 (1995) 869.
[29] I.E. Barton, The entrance effect of laminar flow over a backward-facing step geometry, Int. J. Numer. Methods Fluids 25 (1997) 633.
[30] J.H. Ferziger, M. Perić, Computational Methods for Fluid Dynamics, Springer, New York, 1999.
[31] U. Ghia, K.N. Ghia, C.T. Shin, High-Re solutions for incompressible flow using the Navier–Stokes equations and a multigrid method, J. Comput. Phys. 48 (1982) 387.

[32] S. Hou, Q. Zou, S. Chen, G. Dollen, A.C. Cogley, Simulation of cavity flow by the lattice Boltzmann method, J. Comput. Phys. 118 (1995) 329.
[33] F. Nieuwstadt, H.B. Keller, Viscous flow past circular cylinders, Comput. Fluids 1 (1973) 59.
[34] B. Fornberg, A numerical study of steady viscous flow past a circular cylinder, J. Fluid Mech. 98 (1980) 819.
[35] Y. Saad, Iterative Methods for Sparse Linear Systems, PWS, 1996.
[36] P. Beaudan, Numerical experiments on the flow past a circular cylinder at sub-critical Reynolds number, Ph.D Thesis, Stanford University, 1994.
[37] R. Bouard, M. Coutanceau, The early stage of development of the wake behind an impulsively started cylinder for $40 < Re < 10^4$, J. Fluid Mech. 101 (1980) 583.